MODELLING AND DESIGN OF COLD-FORMED S960 STEEL BRACE-ROTATED TUBULAR T- AND X-JOINTS

Madhup Pandey[1,*] and Ben Young[2]

[1]*Department of Civil Engineering, University of Nottingham, Nottingham, United Kingdom.*
[2]*Department of Civil and Environmental Engineering, The Hong Kong Polytechnic University, Hong Kong, China.*

Abstract

This paper presents detailed numerical investigation and design of cold-formed S960 steel grade brace-rotated (BR) tubular T- and X-joints. The BR tubular joint is one of the novel bird-beak tubular joint configurations, where the rotation of brace member(s) enhances joint resistance and aesthetic appearance. The numerical investigation was performed through finite element (FE) analysis. The tests carried out by the authors were used to develop accurate FE models of BR T- and X-joints, which in turn precisely replicated the joint resistances, load vs deformation curves and failure modes of test specimens. With an aim to broaden the data size, a comprehensive FE parametric study was performed using the verified FE models. The nominal resistances predicted from the literature and European code were compared to the joint failure resistances of 211 BR T- and X-joints specimens, including 192 FE specimens investigated in this study. The BR T- and X-joint specimens were failed by two failure modes, namely chord face failure (F) mode and a combination of chord face and chord side wall failure mode, i.e. combined failure (F+S) mode. It has been shown that the existing design provisions are unsuitable for the design of cold-formed S960 steel grade BR T- and X-joints investigated in this study. Hence, using three design approaches, accurate, less dispersed, reliable and user-friendly design equations are proposed in this study to estimate the joint failure resistances of cold-formed S960 steel grade BR T- and X-joints.

Keywords: Brace-rotated joints; Cold-formed steel; Design provisions; FE analysis; High strength steel; Tubular joints.

---

*Corresponding author. (e-mail: madhup.pandey@nottingham.ac.uk).

1. Introduction

Brace-rotated (BR) tubular joints are obtained by rotating the brace members of conventional RHS-to-RHS joints about their centroidal axes, where RHS represents both square and rectangular hollow sections. The rotation of brace about the centroidal axis increases its effective width, which in turn enhances the joint resistance without further increasing the material and fabrication costs. In addition to the flat connecting end of brace member, the overall welding operation of a BR joint is relatively easier than that of RHS-to-RHS joints. Moreover, brace rotation provides relatively less hindrance for wind and wave loads compared to conventional RHS-to-RHS joint. These merits of brace rotation promote the application of these joints in structures subjected to different types of loading, including topsides and jackets of offshore structures, agricultural equipment, booms and jibs of cranes, wheels, bridges, towers, trusses, spatial structures, stadiums, buildings, prefabricated modular structures and so on. A wide range of analytical, experimental and numerical investigations were carried out on different types of conventional tubular joints in the last six decades. Design rules were subsequently proposed to predict the static resistances of conventional tubular joints made of normal strength steel (in this study, referred to steels with steel grades lower than or equal to S460). In order to extend the applicability of design rules for high strength steel (HSS) (in this study, referred to steels with steel grades higher than S460), the design rules are required to be multiplied by the recommended material factors (C_f).

HSS hollow section members are in high demand in various civil engineering projects due to high strength-to-weight ratio, reduced handling cost and reduced erection time. However, the lack of adequate research work and design recommendations are the primary reasons hampering the widespread use of HSS tubular members. However, some studies have recently been conducted to investigate the static behaviour of cold-formed high strength steel (CFHSS) tubular T- and X-joints [1-7]. To the best of the authors' knowledge, only three studies are available for the BR joints in the literature [1,2,8]. The BR configuration with SHS braces was first studied by Bae et al. [8] through both analytical and experimental methods. In total, 21 tests were carried out by Bae et al. [8] to investigate the ultimate resistances of BR T-joints made of S235 steel grade SHS members. Design rules were then proposed for predicting the ultimate resistances of the investigated BR T-joints.

Pandey and Young [1,2] conducted experimental investigations on cold-formed S960 steel grade BR T- and X-joints, where BR joints were fabricated using both square and rectangular hollow sections (SHS and RHS) brace members. The brace-rotation angle (ω) in Bae et al. [8] was limited to 45°, however, ω ranged from 27° to 63° in Pandey and Young [1,2]. The static resistances of cold-formed high strength steel (CFHSS) BR T- and X-joints undergoing compression loads were investigated by Pandey and Young [1,2]. In order to develop a comprehensive understanding of the static behaviour of CFHSS BR T- and X-joints, a detailed numerical investigation was performed in this study. The test [1,2] and numerical resistances were compared with the nominal resistances predicted from design rules given in Bae et al. [8] as well as with the nominal resistances predicted from RHS-to-RHS and circular hollow section (CHS)-to-RHS design rules given in EC3 [9]. It has been demonstrated that the existing design rules were unsuitable for the range of BR T- and X-joints investigated in this study. As a result, accurate, less dispersed and reliable design equations are proposed, using three design approaches, to predict the joint failure resistances (N_f) of cold-formed S960 steel grade BR T- and X-joints. The joint failure resistance (N_f) of BR T- and X-joints has been defined as the load corresponding to the first occurrence of ultimate resistance (i.e. peak load) (N_{max}) and the load at 3% chord connecting face indentation (i.e. $0.03b_0$) in the load (N) vs chord face indentation (u) curve.

2. Brief description of experimental investigations

The joint failure resistances (N_f) and ultimate resistances (N_{max}) of cold-formed BR T- and X-joints made of S960 steel grade were investigated by Pandey and Young [1,2]. Axial compression loads were applied on BR T- and X-joints test specimens through brace members. The chord ends of BR T-joint test specimens were supported on rollers through bearing blocks. On the other hand, for BR X-joint test specimens, top brace end was fixed and vertical displacement was allowed at the bottom brace end. The braces and chords were made of S960 steel grade RHS members. The thermo-mechanically controlled processed plates of S960 steel grade were cold-formed to obtain hollow section members. A fully robotic metal active gas welding process was used to weld brace and chord members. In total, 19 tests were conducted, including 10 BR T-joints and 9 BR X-joints. Moreover, chord ends were not welded to end plates and freely deformed during the tests. Fig. 1(a) presents various notations for BR T-joint, which are also valid for BR X-joint. The static behaviour of BR T- and X-joints primarily depend on non-dimensional geometric ratios, including β' ($=b_1^{'}/b_0$), 2γ ($=b_0/t_0$), τ ($=t_1/t_0$) and h_0/t_0. The symbols b, h, t and R stand for cross-section width, depth, thickness and external corner radius of RHS member, respectively. The subscripts 0 and 1 denote chord and brace members, respectively.

In the test programs [1,2], β' varied from 0.53 to 0.88, 2γ varied from 25.3 to 38.8, h_0/t_0 varied from 25.4 to 38.9 and τ varied from 0.67 to 1.28. The lengths of brace members (L_1) of BR T- and X-joints were determined as $2\sqrt{b_1^2+h_1^2}$ mm. On the other hand, the lengths of chord members (L_0) of BR T- and X-joints were determined as $h_1^{'}+3h_0+180$ mm and $h_1^{'}+4h_0$ mm, respectively. The symbols $b_1^{'}$ and $h_1^{'}$ represent effective width and depth of brace cross-section, respectively. For SHS brace, $b_1^{'}$ and $h_1^{'}$ are equal to $\sqrt{b_1^2+h_1^2}-0.83R_1$. However, for RHS brace, $b_1^{'}$ and $h_1^{'}$ are equal to $2\max[b_1,h_1]\sin\omega-0.83R_1$ and $\sqrt{b_1^2+h_1^2}-0.83R_1$, respectively. The measured static yield strengths of tubular members ranged from 952 to 1059 MPa, while the measured static yield strength of welding filler material was 965 MPa. The BR T- and X-joint test specimens were failed by two failure modes, namely chord face failure (F) mode and a combination of chord face and chord side wall failure mode, i.e. combined failure (F + S) mode. The test results were obtained in the form of N vs u curves, where N and u respectively denote static load and chord face indentation. The testing machine was paused for 120 seconds at two different locations in each test. The load drops captured during the pauses were used to convert the test curves into static curves. Consequently, the obtained test results were free from the influence of the applied loading rate.

3. Numerical program

3.1. Finite element models of brace-rotated (BR) T- and X-joints

3.1.1. Introduction

One of the popular finite element software, ABAQUS [10], was used to perform the numerical investigation in this study. The static (general) analysis procedure given in ABAQUS [10] was used as the solver. As the induced strains in the finite element (FE) models during the applied loads were unidirectional (i.e. no load reversal), the isotropic strain hardening law was selected for the analysis. The von-Mises yield criterion is generally the default criterion used to predict the onset of yielding in most metals, except for porous metals. Therefore, the yielding onsets of FE models in this study were based on the von-Mises yield theory. In the FE analyses, the growth of the time step was kept non-linear to reduce the overall computation time. Furthermore, the default Newton-Raphson method was used to find the roots of non-linear equilibrium equations. In addition to the accuracy associated with the Newton-Raphson method, one of the popular benefits of using this numerical technique is its quadratic convergent approach, which in turn significantly increases the convergence rate of non-linear problems.

The material non-linearity was considered in the FE models by assigning the measured values of static stress-strain curves of flat and corner regions of RHS members in the plastic material definition part of the FE models. However, prior to the inclusions of experimentally obtained constitutive material curves in the FE models, they were first converted into static curves, and then transformed into true stress-strain curves. On the other hand, the geometric non-linearities in FE models were included by enabling the non-linear geometry parameter (*NLGEOM), which in turn allow FE models to undergo large displacement during the analyses. Furthermore, various factors, including through-thickness division, contact interactions, mesh seed spacing, corner region extension and element types, were also studied and discussed in the following sub-sections of this paper. The labelling of parametric BR T- and X-joint FE specimens was kept identical to the label system used in the test programs [1,2]. The values of ω adopted in the FE parametric study are shown in Fig. 1(b).

3.1.2. Material properties, element type and mesh seed spacing

The test specimens [1,2] were fabricated from tubular members that belonged to the identical batch of tubes used by Pandey and Young [11]. Additionally, Pandey and Young [12] investigated the material properties of welding filler material. The details pertaining to the material properties of welding filler material and tubular members can be referred to Pandey and Young [11,12]. The inclusions of static stress-strain curves in FE models helped averting the effect of loading rate from FE results. The true stress-strain curves of welding filler material as well as flat and corner portions of RHS members were assigned to the corresponding parts of the FE specimens. In this study, the influence of cold-working in RHS members was included in FE models by assigning wider corner regions. Various distances for corner extension in RHS members were considered in the sensitivity analyses, and finally, the corner portions were extended by $2t$ into the neighbouring flat portions, which was in agreement with other studies conducted on CFHSS tubular members and joints (Ma et al. [13,14] and Pandey et al. [15,16]). Except for the welds, all other parts of the FE models were developed using the C3D20 element. On the other hand, the C3D10 element was used to model the weld parts due to their complicated shapes. The weld parts were freely meshed using the free-mesh algorithm, while brace and chord parts were meshed using the structure-mesh algorithm. The use of solid elements helped in making realistic fusions between tubular and weld parts of BR T- and X-joints FE models.

Convergence studies were conducted using different mesh sizes, and finally, chord and brace members were seeded at 4 mm and 7 mm intervals, respectively, along both longitudinal and transverse directions. Moreover, the seeding intervals of weld parts reciprocated the seeding spacings of their respective brace parts. In order to ensure the smooth transfer of stresses between the flat regions of RHS cross-section, the corner regions of RHS cross-section were split into ten elements. FE analyses were also conducted to examine the influence of divisions along the wall thickness of RHS members. The results of these FE analyses demonstrated the trivial influence of wall thickness divisions on the load vs chord face indentation curves of the investigated BR T- and X-joints. The use of the C3D20 element as well as the small wall thickness of test specimens, led to such observations. It is worth noting that a similar observation was also noticed in other studies (Pandey et al. [15,16] and Crockett [17]). Thus, for the validations of BR T- and X-joints FE models, the wall thicknesses of tubular members were kept unsplit.

3.1.3. Weld modelling and contact interactions

Fillet welds were modelled around the junctions of BR T- and X-joints. According to the prequalified weld details of tubular joints given in AWS D1.1M [18], the weld leg sizes of the fillet welds were designed as 1.5 times the minimum of brace and chord wall thickness. The welds were modelled using the average values of measured weld sizes, which are reported in Pandey and Young [1,2]. The inclusions of weld geometries and weld material properties appreciably improved the overall accuracies of BR T- and X-joints FE models. In addition, modelling of weld parts facilitated in realistic load transfer between brace and chord members, which in turn helped in obtaining actual joint behaviour. The selection of the C3D10 element maintained optimum stiffness around the joint perimeter due to its ability to take complicated shapes. A total of two types of contact interactions was defined in BR T- and X-joints FE models. First, contact interaction between brace and chord members of BR T- and X-joints FE models. Second, contact interaction between chord members and bearing blocks of BR T-joint FE models. In addition, a tie constraint was also established between weld and tubular members of BR T- and X-joints FE models. Both contact interactions were established using the built-in surface-to-surface contact definition.

The contact interaction(s) between brace and chord members of BR T- and X-joints FE models was kept frictionless, while a frictional penalty equal to 0.3 was imposed on the contact interaction between chord member and bearing blocks of BR T-joint FE models. Along the normal direction of these two contact interactions, a 'hard' contact pressure overclosure was used. In addition, finite sliding was permitted between the interaction surfaces. For contact interactions and tie constraint, the surfaces were connected to each other using the 'master-slave' algorithm technique. This technique permits the separation of fused surfaces under tension, however, it does not allow penetration of fused surfaces under compression. This technique of fusion between various parts of FE models has been successfully used in several other investigations (Pandey et al. [15,16]; Lan et al. [19]; Li and Young [20]; Li and Young [21,22]). For the brace-chord interaction, the cross-section surface of the brace connected to the chord member was assigned as the 'master' region (relatively less deformable), while the chord connecting surface was assigned as the 'slave' region (relatively more deformable). For the chord-bearing block interaction, the chord member was assigned as the 'slave' region, while the bearing block was assigned as the 'master' region. For the weld-tubular member tie connection, the weld surfaces were assigned as the 'master' regions, while the connecting brace and chord surfaces were assigned as the 'slave' regions.

3.1.4. Boundary conditions and load applications

The boundary conditions in BR T- and X-joints FE models were assigned through reference points. Three reference points were created for the BR T-joint FE model, including one top reference point (TRP) and two bottom reference points (BRP-1 and BRP-2). The TRP replicated the fixed boundary condition of the top brace end, while BRP-1 and BRP-2 replicated the boundary conditions of rollers positioned at both chord ends. As shown in Fig. 2, the TRP was created at the cross-section centre of the top brace end, while BRP-1 and BRP-2 were created at 20 mm below the centre of the bottom surfaces of bearing blocks. The TRP, BRP-1 and BRP-2 were then coupled to their corresponding surfaces using the built-in kinematic coupling type. In order to exactly replicate the boundary conditions of the BR T-joint test setup, all degrees of freedom (DOF) of TRP were restrained. On the other hand, for BRP-1 and BRP-2, except for the translations along the vertical and longitudinal directions of the BR T-joint FE specimen as well as the rotation about the transverse direction of the chord member, all other DOF of BRP-1 and BRP-2 were also restrained. In addition, all DOF of other nodes of BR T-joint FE specimen were kept unrestrained for both rotation and translation.

With regard to the BR X-joint FE model, the top and bottom reference points (TRP and BRP) were created at the cross-section centres of the top and bottom brace members, as shown in Fig. 3. Subsequently, TRP and BRP were coupled to their respective brace end cross-section surfaces using the kinematic coupling type. In order to exactly replicate the boundary conditions of the BR X-joint test setup, all DOF of TRP were restrained. However, except for the translation along the vertical direction of the BR X-joint specimen, all other DOF of BRP were also restrained. Moreover, all DOF of other nodes of the BR X-joint FE specimen were kept unrestrained for both rotation and translation.

Using the displacement control method, compression load was then applied at the bottom reference points of the BR T- and X-joints FE models. In addition, the size of the step increment was kept small to obtain smooth load vs chord face indentation curves. Following this approach, the boundary conditions and load application in FE models were identical to the test programs [1,2].

3.1.5. Weld heat affected region (WHAR)

The heat transferred to parent tubular members during the welding process has a considerable influence on the overall behaviour of hollow section joints [15,16]. The design rules in international standards/guidelines (EC3 [9]; AISC 360 [23]; ISO 14346 [24]; IIW [25]; CIDECT [26]) are identical for HSS produced from different methods, namely by adding alloying elements and by various heat treatment techniques. However, it has been reported in some recent studies [27-30] that HSS produced by different methods exhibited different extents of softening around the welds. Investigations carried out by Stroetmann et al. [27], Javidan et al. [28] and Amraei et al. [29,30] reported 16% to 32% reductions in the ultimate strengths of S960 steel grade parent materials around the welds. The material properties of weld heat affected region (WHAR) of S960 steel grade tubular members with wall thickness ranged from 3 to 6 mm were investigated by Pandey and Young [5]. A 14% to 32% reduction in the ultimate strengths of the parent metals was reported by Pandey and Young [5] in the first 6 mm distance of the WHAR. The definition of WHAR for tubular joints was proposed by Pandey et al. [15], as shown in Fig. 4. For BR T- and X-joints FE models, the spreads of WHAR are shown in Figs. 2 and 3, respectively. In addition, a simplified strength reduction (S_{rl}) model was proposed by Pandey et al. [15] for S900 and S960 steel grades tubular joints to integrate the material properties of WHAR in FE models, as illustrated in Fig. 5. The proposed strength reduction model was successfully used to perform the numerical investigation and design of CFHSS T- and TF-joints (Pandey et al. [15,16]). Therefore, it was also included in this investigation, and accordingly, material properties were assigned to the WHAR of BR T- and X-joints FE models. The adoption of WHAR appreciably improved the accuracies of FE models, and thus, the numerical results.

3.2. Validations of BR T- and X-joints FE models

The numerical modelling techniques described in the preceding section of this paper were used to develop BR T- and X-joints FE models. The test results of BR T- and X-joints reported in Pandey and Young [1,2] were used to validate their corresponding FE models. The validations were performed by duly comparing the N_f, N_{max}, N vs u curves and failure modes of test and FE specimens. The measured dimensions of tubular members and welds were used to develop all BR T- and X-joints FE models. In addition, measured material properties of tubular members, welds and WHAR were also included. The N_f and N_{max} of BR T- and X-joints test specimens were compared with those predicted from their corresponding FE models ($N_{f,FE}$ and $N_{max,FE}$), as shown in Tables 1 and 2, respectively. Referring to Table 1, when the joint failure resistances of BR T-joint ($N_{f,T}$) test specimens were compared with the resistances predicted from BR T-joint FE models, the mean (P_m) and coefficients of variation (COV) (V_p) of the comparisons were 1.01 and 0.014, respectively. However, when the ultimate resistances of BR T-joint ($N_{max,T}$) test specimens were compared with the FE resistances, the P_m and V_p of the comparisons were 1.00 and 0.017, respectively.

On the other hand, as shown in Table 2, when the joint failure resistances of BR X-joint ($N_{f,X}$) test specimens were compared with the resistances predicted from BR X-joint FE models, the P_m and V_p of the comparisons were 1.01 and 0.023, respectively. However, when the ultimate resistances of BR X-joint ($N_{max,X}$) test specimens were compared with the FE resistances, the P_m and V_p of the comparisons were 1.02 and 0.021, respectively. Likewise, the experimental investigation, the N_f of BR T- and X-joints FE specimens was determined by jointly considering the ultimate resistances and ultimate deformation limit (i.e. $0.03b_0$) loads, whichever occurred earlier in the N vs u curves. In addition, the comparisons of N vs u curves between typical BR T- and X-joints test and FE specimens are shown in Figs. 6 and 7, respectively. Moreover, Figs. 8 and 9 present the comparisons of failure modes between typical BR T- and X-joints test and FE specimens, respectively. Therefore, from Tables 1-2 and Figs. 6-9, it can be concluded that the validated FE models precisely replicated the overall static behaviour of BR T- and X-joints investigated in this study.

3.3. Parametric FE modelling of BR T- and X-joints

3.3.1. General

The data pool was widened by performing a comprehensive numerical parametric study using the validated BR T- and X-joints FE models. In total, 192 parametric FE analyses were performed in this study, including 96 BR T-joints and 96 BR X-joints. Table 3 presents the ranges and values of various critical parameters considered in the parametric study. All FE modelling techniques used in the validations of BR T- and X-joints were also employed in the parametric study. It is important to mention that, in this investigation, the N_f of all BR T- and X-joints parametric FE specimens were controlled by the ultimate deformation limit (i.e. $0.03b_0$) criterion.

3.3.2. Specifications for parametric FE modelling of BR T- and X-joints

In the numerical investigation, the dimensions of tubular members included practical sizes. Overall, the values of cross-section width and depth of brace and chord members of parametric FE specimens ranged from 40 mm to 200 mm, while their wall thickness ranged from 2.5 mm to 12 mm. The exterior corner radii of brace and chord members (R_1 and R_0) conformed to the commercially produced HSS members (SSAB [31]). In this study, R_1 and R_0 were kept as $2t$ for $t \leq 6$ mm, $2.5t$ for $6 < t \leq 10$ mm and $3t$ for $t > 10$ mm, which in turn also met the limits detailed in EN 10219-2 [32]. The lengths of braces and chords of BR T- and X-joints FE specimens were determined using the formulae that were also used to design the test specimens [1,2], as mentioned in Section 2 of this paper. For meshing along the longitudinal and transverse directions of RHS members, seedings were approximately spaced at the minimum of $b/30$ and $h/30$, where b and h stand for cross-section width and depth of the RHS member. Overall, the adopted mesh sizes of parametric FE specimens ranged from 3 mm to 10 mm. On the other hand, the seeding interval of weld parts of parametric FE specimens reciprocated the seeding interval of their corresponding brace parts. For precise replication of RHS curvatures, the corner regions of braces and chords were split into ten elements. Likewise, in the validation process, the corner regions of RHS members were extended by $2t$ into their neighbouring flat portions. For FE specimens with $t \leq 6$ mm, no divisions were made along the wall thicknesses of brace and chord members. However, when $t > 6$ mm, the wall thicknesses of brace and chord members were divided into two layers. The design of fillet weld leg sizes for both BR T- and X-joints FE specimens was consistent with the design adopted in the test programs [1,2]. In the parametric study, the material properties of flat and corner portions of RHS 150×150×6 were assigned to the flat and corner regions of brace and chord members of FE specimens. Besides, weld parts of all BR T- and X-joints parametric FE specimens were given the measured material properties of welding filler material. Table 4 presents the measured material properties of RHS 150×150×6 and welding filling material adopted in the parametric study, which include Young's modulus (E), 0.2% proof stress and strain ($\sigma_{0.2}$ and $\varepsilon_{0.2}$), ultimate stress and strain (σ_u and ε_u), fracture strain (ε_f) and Ramberg-Osgood parameter (n). On the other hand, the material properties and spread of WHAR were in accordance with the recommendations proposed by Pandey et al. [15].

3.3.3. Failure modes of BR T- and X-joints

The BR T- and X-joints test and FE specimens were failed by two failure modes, namely chord face failure (F) mode, and a combination of chord face and chord side wall failure mode, i.e. combined failure (F+S) mode. Overall, the BR T- and X-joints specimens were failed by the F mode when $\beta' \leq 0.85$. On the other hand, the F+S mode occurred for the BR T- and X-joints test and FE specimens when $\beta' > 0.85$. It is important to note that both these failure modes were defined corresponding to the N_f, which in turn was computed by jointly considering the ultimate and $0.03b_0$ limit loads. The test and parametric FE specimens were failed by the F mode, when the N_f was determined using only the ultimate deformation limit ($0.03b_0$) load criterion. The applied loads of BR T- and X-joints specimens that failed by the F mode were monotonically increasing with the increase of chord face indentation. For BR T- and X-joints test and FE specimens that failed by the F+S mode, the load vs chord face indentation curves exhibited a visible peak load (i.e. ultimate resistance). Additionally, evident deformations of chord flange, chord webs and chord corner regions were noticed in the test and parametric FE specimens that failed by the F+S mode. Moreover, none of the test and FE specimens were failed by the global buckling of brace members.

4. Existing design provisions

The BR T- and X-joints are currently not covered in any international code and guideline. In the literature, design rules are only available for S235 steel grade BR T-joint (Bae et al. [8]). The overall static performance of tubular T- and X-joints when subjected to axial compression loads through brace members are nearly similar. Therefore, in this investigation, the N_f of both BR T- and X-joints test and parametric FE specimens were evaluated against the nominal resistances predicted from the design rules proposed by Bae et al. [8]. Moreover, the BR joint configuration partially resembles to that of conventional RHS-to-RHS (due to orientation of chord) and CHS-to-RHS (due to orientation of brace) configurations. Thus, the N_f of BR T- and X-joints test and parametric FE specimens were also evaluated against the nominal resistances of RHS-to-RHS and CHS-to-RHS T- and X-joints design rules given in EC3 [9]. The measured dimensions and material properties of tubular members were used to calculate the nominal resistances. Under axial compression load, the chord members of BR T-joints were subjected to chord-in-plane bending. In this investigation, the effect of normal stresses developed due to chord-in-plane bending on the static resistances of BR T-joints was considered through the chord stress function (Q_f). On the other hand, in this study, no preload was applied to the chord members of BR X-joints. Therefore, the value of Q_f for BR X-joints was set to unity in Eqs. (3) to (6). Furthermore, as design equations proposed by Bae et al. [8] were valid for S235 steel grade BR T-joints, thus, the nominal resistances predicted from Bae et al. [8] were multiplied by a material factor (C_f) equal to 0.80 to facilitate their evaluations against the test and FE resistances of cold-formed S960 steel grade BR T- and X-joints.

4.1. Bae et al. [8]

Bae et al. [8] proposed design equations (Eqs. (1) and (2)) to estimate the ultimate resistances of S235 steel grade BR T-joints subjected to compression loads through brace members. The proposed design equations are valid for $0.38 \leq \beta' \leq 1.0$ and $16.7 \leq 2\gamma \leq 33.3$.

Chord face failure ($\beta' \leq 0.85$)

$$N_{Bae} = \frac{f_{y0} t_0^2}{4} \left[10 + \frac{4(1+\beta')}{(1-\beta')} \right] \tag{1}$$

Chord web failure ($\beta' = 1.0$)

$$N_{Bae} = 2 f_k t_0 \left(0.89 b_1\right) \quad (2)$$

In order to extend the applicability of Eqs. (1) and (2) for CFHSS BR joints investigated in this study, a material factor (C_f) equal to 0.80 should be included in Eqs. (1) and (2). The nominal resistances determined after including the C_f factor in Eqs. (1) and (2) are represented by $N^{\wedge}_{Bae}$.

4.2. EC3 [9]

The design rules given in EC3 [9] are applicable for tubular joints with steel grades up to S700. However, a material factor (C_f) is required to be multiplied to the design rules when steel grade exceeds S355. When steel grade ranged from 550 to 700 MPa, the value of material factor (C_f) is equal to 0.80. Furthermore, EC3 [9] has explicitly recommended the value of partial safety factor for tubular joints (γ_{M5}), which is equal to 1.0. The design equations for chord face failure and chord side wall failure modes are shown below:

<u>RHS-to-RHS T- and X-joints:</u>

Chord face failure ($\beta \leq 0.85$):

$$N^{\wedge}_{E,RR} = \frac{C_f}{\gamma_{M5}} Q_f \frac{f_{y0} t_0^2}{\sin\theta_1} \left(\frac{2\eta}{(1-\beta)\sin\theta_1} + \frac{4}{\sqrt{1-\beta}} \right) \quad (3)$$

Chord side wall failure *($\beta = 1.0$)*:

$$N^{\wedge}_{E,RR} = \frac{Q_f}{\gamma_{M5}} \frac{f_b t_0}{\sin\theta_1} \left(\frac{2h_1}{\sin\theta_1} + 10 t_0 \right) \quad (4)$$

<u>CHS-to-RHS T- and X-joints:</u>

Chord face failure ($\beta' \leq 0.85$):

$$N^{\wedge}_{E,CR} = \frac{\pi}{4} \frac{C_f}{\gamma_{M5}} Q_f \frac{f_{y0} t_0^2}{\sin\theta_1} \left(\frac{2\left(h_1'/b_0\right)}{(1-\beta')\sin\theta_1} + \frac{4}{\sqrt{1-\beta'}} \right) \quad (5)$$

Chord side wall failure ($\beta' = 1.0$):

$$N^{\wedge}_{E,CR} = \frac{\pi}{4} \frac{Q_f}{\gamma_{M5}} \frac{f_b t_0}{\sin\theta_1} \left(\frac{2h_1'}{\sin\theta_1} + 10 t_0 \right) \quad (6)$$

In Eqs. (1) to (6), the term f_{y0} represents the yield strength of chord member, f_k and f_b represent buckling stress of chord member as per EC3 [33]; γ_{M5} is the partial safety factor of tubular joints as per EC3 [9] and θ_1 represents the angle between brace and chord members in degrees.

5. Reliability analysis

In order to examine the reliability of existing and proposed design equations, a reliability study was performed as per AISI S100 [34]. The Eq. (7) was used to calculate the reliability index (β_0). In this investigation, a lower bound value of 2.50 was taken as the target β_0. Therefore, when $\beta_0 \geq 2.50$, the design equation was treated as reliable in this study.

$$\beta_0 = \frac{\ln(C_\phi M_m F_m P_m / \phi)}{\sqrt{V_M^2 + V_F^2 + C_P V_P^2 + V_Q^2}} \tag{7}$$

A dead load (DL)-to-live load (LL) ratio of 0.20 was used to compute the calibration coefficient (C_ϕ) in Eq. (7). For the material factor, the mean value and COV were respectively symbolised by M_m and V_M. For the fabrication factor, the mean value and COV were respectively symbolised by F_m and V_F. Referring to AISI S100 [34], the M_m and V_M were adopted as 1.10 and 0.10, respectively. Additionally, F_m and V_F were adopted as 1.00 and 0.10, respectively. The resistance factor required to convert the nominal resistance to design resistance was denoted by ϕ. The mean value of ratios of test and FE resistances-to-nominal resistances predicted from literature and code was denoted by P_m, while the corresponding COV was denoted by V_P. The correction factor (C_P) proposed by AISI S100 [34] was also used in Eq. (7) to incorporate the effect of the amount of data under consideration. Besides, V_Q symbolised the COV of load effects. In order to evaluate the reliability levels of EC3 [9] design provisions, the DL and LL were combined as 1.35DL + 1.5LL as per EN [35], and thus, the calculated value of C_ϕ was 1.463. Further, to examine the reliability levels of the design equation proposed by Bae et al. [8] as well as for the proposed design rules, the DL and LL were combined as 1.2DL + 1.6LL as per ASCE 7 [36], and the calculated value of C_ϕ was 1.521.

6. Comparisons of joint failure resistances with nominal resistances

The comparisons of N_f of BR T- and X-joints test and FE specimens with nominal resistances are shown in Tables 5 and 6, respectively. The comparisons are also graphically shown in Figs. 10 to 13, 15 and 16. Table 5 presents the comparisons of $N_{f,T}$ of BR T-joint test and parametric FE specimens with nominal resistances predicted from Bae et al. [8] and EC3 [9]. The comparisons results proved that the design rules proposed by Bae et al. [8], RHS-to-RHS and CHS-to-RHS T-joints design rules of EC3 [9] satisfactorily predicted the $N_{f,T}$ of cold-formed S960 steel grade BR T-joints. However, the predictions were very dispersed and the design equations were found to be unreliable. Fig. 10 graphically presents the comparisons of $N_{f,T}$ of BR T-joint test and parametric FE specimens with nominal resistances predicted from Bae et al. [8] and CHS-to-RHS T-joint design rule of EC3 [9]. The comparisons of $N_{f,X}$ of BR X-joint test and parametric FE specimens with nominal resistances predicted from Bae et al. [8] and EC3 [9] are presented in Table 6. The predictions of the design rules proposed by Bae et al. [8] were found to be satisfactory and very dispersed but unreliable for the $N_{f,X}$ of CFHSS BR X-joints. On the contrary, the comparisons of predictions of RHS-to-RHS and CHS-to-RHS X-joints design rules of EC3 [9] with the $N_{f,X}$ of BR X-joints were found to be slightly unconservative, largely dispersed and unreliable. Fig. 11 graphically presents the comparisons of $N_{f,X}$ of BR X-joint test and parametric FE specimens with nominal resistances predicted from Bae et al. [8] and CHS-to-RHS X-joint design rule of EC3 [9].

The design equations proposed by Bae et al. [8] were developed for S235 steel grade BR T-joints. In addition, only SHS members were used as braces of BR T-joints in Bae et al. [8]. Overall, the design equations (Eqs. (1) and (2) of this paper) satisfactorily predicted the N_f of cold-formed S960 steel grade BR T- and X-joints, as reflected from the values of P_m shown in Tables 5 and 6. However, the predictions were very scattered, and thus, the design rules became unreliable. One of the possible reasons for highly scattered predictions could be due to the assumption of yield lines propagation at 45° from brace corners, which is primarily valid for SHS braces with ω =45°. In this investigation, RHS members were also used as the braces of BR T- and X-joints and the values of

ω ranged from 15° to 63°. In addition, one of the important geometric parameters, 2γ ($=b_0/t_0$), which accounts for the slenderness of chord flat region, was not included in Eq. (1). Moreover, the stress-strain curve of S960 steel significantly deviates from that of mild steel (steel grades up to S355). The prolonged elasticity, absence of yield plateau, different extent of strain hardening, and low ultimate-to-yield strength ratio can change the response of HSS tubular joints, especially in the deformation and propagation of chord face yield line patterns and development of chord face membrane action, compared to the mild steel counterparts [15,37]. For small to medium values of β ratio (i.e. $\beta \leq 0.75$), normal strength steel T- and X-joints are expected to undergo relatively larger chord connecting face deformation compared to corresponding HSS counterparts at the same load level. For HSS T- and X-joints with small to medium values of β ratio (i.e. $\beta \leq 0.75$), and especially for large values of 2γ ratio, the current $0.03b_0$ deformation limit seems not sufficient to develop plastic hinges in the chord connecting face. Therefore, the strength of HSS material from the proportional limit to yield strength could not be effectively utilised owing to the existing $0.03b_0$ deformation limit criterion [15].

7. Proposed design rules

In order to estimate the N_f of cold-formed S960 steel grade BR T- and X-joints, design rules are proposed in this study using three design approaches. Under the first approach, named as proposal-1, new design equations are proposed to predict the N_f of CFHSS BR T- and X-joints. Under the second approach, named as proposal-2, the N_f of CFHSS BR T- and X-joints are predicted by applying a correction factor on the current CHS-to-RHS T- and X-joints design rule (Eq. (5)) given in EC3 [9]. Under the third approach, named as proposal-3, a design equation has been proposed using a simplified yield line model to predict the N_f of CFHSS BR T- and X-joints investigated in this study. Furthermore, as welds were modelled in all parametric FE specimens, the effects of weld and associated WHAR were implicitly included in the proposed design equations. In order to calculate the design resistances (N_d), the proposed nominal resistances (N_{pn1}, N_{pn2} and N_{pn3}) in the following sub-sections of this paper shall be multiplied by their correspondingly recommended resistance factors (ϕ), i.e. $N_d = \phi$ (N_{pn1} or N_{pn2} or N_{pn3}). The design rules proposed in this study are valid for $0.20 \leq \beta \leq 0.67$, $0.26 \leq \beta' \leq 0.88$, $16.6 \leq 2\gamma \leq 40$, $0.50 \leq \tau \leq 1.28$, $15° \leq \omega \leq 63°$ and θ_1=90°.

7.1. Proposal-1 (Unified design equation)

The parameters β', 2γ, h_0/t_0 and τ demonstrated a considerable influence on the static behaviour of BR T- and X-joints. Thus, new design equations (i.e. Eqs. (8) and (9)) are proposed to estimate the N_f of cold-formed S960 steel grade BR T- and X-joints by duly considering the effect of important geometric parameters as well as the P_m and V_p of the overall comparison.

<u>For BR T-joint:</u>

$$N_{pn1} = \frac{f_{y0}t_0^2 e^{2\beta'}\left(\tau + 0.7\right)}{\left[0.6 + 0.01\left(2\gamma\right)\right]\left[0.5 + 0.02\left(\frac{h_0}{t_0}\right)\right]} \tag{8}$$

<u>For BR X-joint:</u>

$$N_{pn1} = \frac{f_{y0}t_0^2 e^{2.3\beta'}\left(0.6\tau + 0.7\right)}{\left[0.4 + 0.017\left(2\gamma\right)\right]\left[0.5 + 0.02\left(\frac{h_0}{t_0}\right)\right]} \tag{9}$$

As shown in Table 5, the P_m and V_p of the proposed design equation for BR T-joint (i.e. Eq. (8)) are 1.00 and 0.149, respectively. On the other hand, referring to Table 6, the P_m and V_p of the proposed design equation for BR X-joint (i.e. Eq. (9)) are 1.04 and 0.160, respectively. For both Eqs. (8) and (9), ϕ equal to 0.80 was recommended, resulting in β_0 equal to 2.52 and 2.57, respectively. Thus, Eqs. (8) and (9) must be multiplied by ϕ equal to 0.80 to get their corresponding design resistances (N_d). The comparisons of N_f of BR T- and X-joints test and FE specimens with nominal resistances predicted from Bae et al. [8], CHS-to-RHS design rule of EC3 [9] and proposed design equations under proposal-1 (Eqs. (8) and (9)) are graphically presented in Figs. 10 and 11, respectively. Compared to the existing design provisions, the predictions from Eqs. (8) and (9) are relatively more accurate, less dispersed and reliable for the N_f of CFHSS BR T- and X-joints.

The formats of the proposed new design equations, i.e. Eqs. (8) and (9), are identical. Therefore, an attempt has been made to propose a unified design equation to predict the N_f of cold-formed S960 steel grade BR T- and X-joints. The proposed unified design equation, as shown in Eq. (10), is valid for $0.26 \leq \beta' \leq 0.88$. The values of coefficients (A to G) are given in Table 7.

$$N_{pn1} = f_{y0} t_0^2 \frac{e^{\mathrm{A}\beta'}\left(\mathrm{B}\tau + \mathrm{C}\right)}{\left[\mathrm{D} + \mathrm{E}\left(2\gamma\right)\right]\left[\mathrm{F} + \mathrm{G}\left(\frac{h_0}{t_0}\right)\right]} \tag{10}$$

7.2. Proposal-2 (Simplified design equations)

Under proposal-2, a correction factor based on geometric parameter 2γ was applied on the current CHS-to-RHS T- and X-joints design rules given in EC3 [9], as shown in Eqs. (11) and (12), to predict the N_f of cold-formed S960 steel grade BR T- and X-joints.

<u>For BR T-joint:</u>

$$N_{pn2} = \left[1.39 - 0.02\left(2\gamma\right)\right] N^{\wedge}_{E,CR} \tag{11}$$

<u>For BR X-joint:</u>

$$N_{pn2} = \left[1.52 - 0.025\left(2\gamma\right)\right] N^{\wedge}_{E,CR} \tag{12}$$

The term $N^{\wedge}_{E,CR}$ in Eqs. (11) and (12) can be obtained from Eq. (5). As shown in Table 5, the P_m and V_p of the proposed design equation for BR T-joint (i.e. Eq. (11)) are 1.05 and 0.182, respectively. On the other hand, referring to Table 6, the P_m and V_p of the proposed design equation for BR X-joint (i.e. Eq. (12)) are 1.06 and 0.187, respectively. For both Eqs. (11) and (12), ϕ equal to 0.80 was recommended, resulting in β_0 equal to 2.51. Thus, Eqs. (11) and (12) must be multiplied by ϕ equal to 0.80 to get their corresponding design resistances (N_d). The comparisons of N_f of BR T- and X-joints test and FE specimens with nominal resistances predicted from Bae et al. [8], CHS-to-RHS design rule of EC3 [9] and proposed design equations under proposal-2 (Eqs. (11) and (12)) are graphically presented in Figs. 12 and 13, respectively. Compared to the existing design provisions, the predictions from Eqs. (11) and (12) are relatively more accurate, less dispersed and reliable for the N_f of CFHSS BR T- and X-joints.

7.3. Proposal-3 (Yield line model)

A simplified yield line model based on the deformed shape of chord connecting face(s) of BR T- and X-joint test specimens [1,2] is proposed in this study, as shown in Fig. 14. The yield line theory is based on the principle of virtual work. Accordingly, the work done by the external forces is equal to the internal work done by the yield lines. In the proposed model, the yield lines propagate along α (degrees) from the brace corners, and after reaching the chord corners, the yield lines further deviate by λ (degrees). Using the principle of virtual work, the design equation to predict the nominal resistances of BR T- and X-joints can be derived as follows:

Total external work done (W_e) = External force (N) × deformation (δ) = $N\delta$

Total internal work done (W_i) = $\sum_{i=1}^{n}\left(M_p\theta_i\right) l_i$

where M_p denotes plastic moment per unit length of the yield line and equal to $f_{y0}t_0^2/4$, θ_i represents the absolute rotation of the i^{th} yield line and l_i stands for the actual length of the yield line under consideration. Using the symmetry of the proposed yield line model as well as for the sake of simplicity, only the left hand side of the model was used to derive the internal work. Referring to Fig. 14, the lengths of yield lines from 1 to 8 are equal to $l_1 = b_0/2\sin\left[90-(\lambda-\alpha)\right]$; $l_2 = x/\cos\alpha$; $l_3 = b_0/2\tan(\lambda-\alpha)+x\tan\alpha$; $l_4 = 2x\tan\alpha$; $l_5 = b_1$; $l_6 = h_1$; $l_7 = h_1\cos\omega+(b_0/2)/\tan(\lambda-\alpha)$; and $l_8 = x/\cos\alpha$, where $x = b_0(1-\beta')/2$. Thus, the total internal work can be calculated as follows:

$$W_i = 2M_p\sum_{i=1}^{8}\theta_i\, l_i = 2M_p\left(\frac{\delta}{p}l_1+\frac{\delta}{l_2}l_2+\frac{\delta}{l_3}l_3+\frac{\delta}{x}l_4+\frac{\delta}{p}l_5+\frac{\delta}{q}l_6+\frac{\delta}{q}l_7+\frac{\delta}{l_8}l_8\right) \tag{13}$$

where p and q respectively represent the average distances of the yield lines l_1 and l_7 from the brace member, and expressed as follows:

$$p = \frac{p_1+p_2}{2} = \frac{1}{2}\left(l_2\sin\lambda + l_3\sin\left[90-(\lambda-\alpha)\right]\right) \tag{14}$$

$$q = \frac{q_1+q_2}{2} = \frac{1}{2}\left(l_3\sin\psi + l_8\sin\left[90-\alpha+\omega\right]\right) \tag{15}$$

By applying a virtual unit displacement, i.e. $\delta = 1$, and substituting the values of l_1 to l_8 and M_p, Eq. (13) can be simplified as:

$$W_i = 2\left[\frac{f_{y0}t_0^2}{4}\left(3 + 2\tan\alpha + \frac{\frac{b_0}{2\sin\left[90-(\lambda-\alpha)\right]} + b_1}{p} + \frac{h_1(1+\cos\omega) + \frac{b_0}{2}\tan(\lambda-\alpha)}{q}\right)\right] \quad (16)$$

In Eq. (15), the angle ψ can be determined as $\psi = \tan^{-1}\left[(b_0/2)/\left\{l_3 + (h_1\cos\omega - x\tan\alpha)\right\}\right]$. A sensitivity analysis was conducted by adopting different values of α and λ. Overall, the joint resistances of BR T- and X-joints test and FE specimens correlated well with α = 40° and λ = 50°, as shown by the values of P_m and V_p in Tables 5 and 6. Therefore, on substituting, α = 40° and λ = 50° in Eq. (16) and equating external and internal work done, the following equation can be obtained.

$$N = \frac{f_{y0}t_0^2}{2}\left\{4.7 + \left(\frac{b_0 + 2b_1}{2p}\right) + \left(\frac{h_1(1+\cos\omega) + 0.1b_0}{q}\right)\right\} \quad (17)$$

It can be noticed that Eq. (17) cannot include one of the important geometric parameters, 2γ ($=b_0/t_0$), which accounts for the slenderness of the chord connecting face(s). Therefore, a reduction factor based on 2γ was applied to Eq. (17) to finally derive the nominal resistance equation for cold-formed S960 steel grade BR T- and X-joints, as follows:

$$N_{pn3} = \left[0.58 - 0.007(2\gamma)\right]\left[f_{y0}t_0^2\left\{4.7 + \left(\frac{b_0 + 2b_1}{2p}\right) + \left(\frac{h_1(1+\cos\omega) + 0.1b_0}{q}\right)\right\}\right] \quad (18)$$

where

$$p = \frac{b_0}{20}(10 - 9\beta') \quad (19)$$

$$q = \frac{b_0}{20}\left[(5 - 4\beta')\sin\psi + \frac{b_0}{3}(1-\beta')\sin(\omega + 50)\right] \quad (20)$$

$$\psi = \tan^{-1}\left(\frac{b_0}{2h_1\cos\omega + \frac{b_0}{5}}\right) \quad (21)$$

The comparisons of N_f of BR T- and X-joints test and FE specimens with corresponding nominal resistances predicted from Eq. (18) are shown in Tables 5 and 6, respectively. As shown in Table 5, the P_m and V_p of Eq. (18) for BR T-joints are 1.02 and 0.215, respectively. On the other hand, referring to Table 6, the P_m and V_p of Eq. (18) for BR X-joints are 1.01 and 0.232, respectively. For Eq. (18), ϕ equal to 0.70 was recommended, resulting in β_0 equal to 2.66 and 2.53 for BR T- and

X-joints, respectively. Thus, Eq. (18) must be multiplied by ϕ equal to 0.70 to get the corresponding design resistances (N_d). The comparisons of N_f of BR T- and X-joints test and FE specimens with nominal resistances predicted from Bae et al. [8], CHS-to-RHS design rule of EC3 [9] and Eq. (18) are graphically presented in Figs. 15 and 16, respectively. Compared to the existing design provisions, the predictions from Eq. (18) are relatively more accurate, less dispersed and reliable for the N_f of CFHSS BR T- and X-joints.

For BR T- and X-joints, the distributions of the comparison ratios of the N_f of test and FE specimens-to-nominal resistances predicted from Bae et al. [8], EC3 [9] and design equations proposed in this study under proposal-1 are shown in Figs. 17 and 18, respectively.

8. Conclusions

The static resistances of cold-formed steel brace-rotated (BR) tubular T- and X-joints were numerically investigated in this study. The braces of BR T- and X-joints were made of square and rectangular hollow sections (SHS and RHS), however, chords were only made of SHS. The nominal 0.2% proof stress of tubular members was 960 MPa. The rotation angle (ω) of brace members ranged from 15° to 63°. The test results reported in Pandey and Young [1,2] were used to develop accurate finite element (FE) models of BR T- and X-joints. An extensive FE parametric study was subsequently performed, which comprised 96 BR T-joints and 96 BR X-joints. The welds and associated weld heat affected regions were included in all FE parametric models, which appreciably improved the accuracy of numerical results. In this study, the joint failure resistances (N_f) of all BR T- and X-joints FE specimens were controlled by the $0.3b_0$ ultimate deformation limit criterion.

The BR T- and X-joints test and FE specimens were failed by two failure modes, namely chord face failure (F) mode and a combination of chord face and chord side wall failure mode, i.e. combined failure (F+S) mode. The design rules given in Bae et al. [8] and EC3 [9] are found to be unsuitable for the design of BR T- and X-joints investigated in this study. As a result, accurate, less dispersed and reliable design equations are proposed, by three design approaches, to predict the joint failure resistances (N_f) of cold-formed S960 steel grade BR T- and X-joints. In the first approach, a unified design equation has been proposed. In the second approach, design equations are proposed by applying correction factors on the existing CHS-to-RHS design rule given in EC3 [9]. However, in the third approach, the design equation is developed using a simplified yield line model. The design equations proposed in this study are valid for $0.20 \leq \beta \leq 0.67$, $0.26 \leq \beta' \leq 0.88$, $16.6 \leq 2\gamma \leq 40$, $0.50 \leq \tau \leq 1.28$, $15° \leq \omega \leq 63°$ and $\theta_1 = 90°$.

Acknowledgement

The work described in this paper was fully supported by a grant from the Research Grants Council of the Hong Kong Special Administrative Region, China (PolyU 15218720).

References

[1] Pandey M and Young B. Ultimate Resistances of Member-Rotated Cold-Formed High Strength Steel Tubular T-Joints under Compression Loads, Engineering Structures 2021;244:112601.

[2] Pandey M and Young B. Effect of Member Orientation on the Static Strengths of Cold-Formed High Strength Steel Tubular X-Joints, Thin-walled Structures 2022;170:108501.

[3] Pandey M and Young B. Structural performance of cold-formed high strength steel tubular X-Joints under brace axial compression. Engineering Structures, 2020; 208:109768.

[4] Pandey M and Young B. Post-Fire Behaviour of Cold-Formed High Strength Steel Tubular T- and X-Joints, Journal of Constructional Steel Research 2021;186:106859.

[5] Pandey M and Young B. Static resistances of cold-formed high strength steel tubular non-90° X-Joints. Engineering Structures 2021;239:112064.

[6] Pandey M and Young B. Stress Concentration Factors of Cold-Formed High Strength Steel Tubular T-Joints, Thin-walled Structures 2021;166:107996.

[7] Pandey M and Young B. Experimental Investigation on Stress Concentration Factors of Cold-formed High Strength Steel Tubular X-Joints, Engineering Structures 2021;243:112408.

[8] Bae KW, Park KS, Choi YH, Moon TS and Stiemer SF. Behavior of branch-rotated T joints with cold-formed square hollow sections. Canadian Journal of Civil Engineering, 7(33), 2006, 827-836.

[9] Eurocode 3 (EC3), Design of Steel Structures-Part 1-8: Design of Joints, prEN 1993-1-8, European Committee for Standardization, CEN, Brussels, Belgium, 2021.

[10] Abaqus/Standard. Version 6.17. USA: K. a. S. Hibbit; 2017.

[11] Pandey M and Young B. Tests of cold-formed high strength steel tubular T-joints. Thin-Walled Struct 2019;143:106200.

[12] Pandey M and Young B. Compression capacities of cold-formed high strength steel tubular T-joints. J Constr Steel Res, 162, 2019:105650.

[13] Ma JL, Chan TM and Young B. Design of cold-formed high strength steel tubular beams. Engineering Structures, 151, 2017, pp.432-443.

[14] Ma JL, Chan TM and Young B. Cold-formed high strength steel tubular beam-columns. Engineering Structures, 230, 2021, p.111618.

[15] Pandey M, Chung KF and Young B. Design of cold-formed high strength steel tubular T-joints under compression loads. Thin-Walled Structures 2021;164:107573.

[16] Pandey M, Chung KF and Young B. Numerical investigation and design of fully chord supported tubular T-joints. Engineering Structures 2021;239:112063.

[17] Crockett P. Finite element analysis of welded tubular connections. PhD Thesis, University of Nottingham, 1994.

[18] AWS D1.1/D1.1M, Structural Welding Code – Steel, American Welding Society (AWS), Miami, USA, 2020.

[19] Lan X, Chan TM and Young B. Structural behaviour and design of high strength steel RHS X-joints. Engineering Structures 2019;200:109494.

[20] Li HT and Young B. Cold-formed stainless steel RHS members undergoing combined bending and web crippling: Testing, modelling and design. Engineering Structures, 250, 2022, 113466.

[21] Li QY and Young B. Design of cold-formed steel built-up open section members under combined compression and bending. Thin-Walled Structures. 2022; 172:108890.

[22] Li QY and Young B. Experimental and numerical investigation on cold-formed steel built-up section pin-ended columns. Thin-Walled Structures. 2022; 170:108444.

[23] ANSI/AISC 360. Specification for Structural Steel Buildings. American Institution of Steel Construction, Chicago, USA; 2016.

[24] ISO 14346. Static design procedure for welded hollow-section joints – Recommendations. British Standard International Standards, Geneva, Switzerland; 2013.
[25] IIW Doc. XV-1402-12 and IIW Doc. XV-E-12-433. Static design procedure for welded hollow section joints – Recommendations. International Institute of Welding, Paris, France, 2012.
[26] Packer JA, Wardenier J, Zhao XL, Vegte GJ van der, Kurobane Y. Design guide for rectangular hollow section (RHS) joints under predominantly static loading. Comite´ International pour le Developpement et l'Etude de la Construction TuECbulaire (CIDECT), Design Guide No. 3, 2nd edn., LSS Verlag, Dortmund, Germany, 2009.
[27] Stroetmann R, Kastner T, Halsig A and Mayr P. Mechanical properties and a new design approach for welded joints at high strength steels. Hong Kong:Engineering Research and Practice for Steel Construction; 2018:79–90.
[28] Javidan F, Heidarpour A, Zhao XL, Hutchinson CR and Minkkinen J. Effect of weld on the mechanical properties of high strength and ultra-high strength steel tubes in fabricated hybrid sections. Eng Struct 2016;118:16–27.
[29] Amraei M., Ahola A., Afkhami S., Bjork T., Heidarpour A. and Zhao X.L. .Effects of heat input on the mechanical properties of butt-welded high and ultra-high strength steels, Engineering Structures, 2019, 198, 109460.
[30] Amraei M., Afkhami S., Javaheri V., Larkiola J., Skriko T., Bjork T. and Zhao X.L. .Mechanical properties and microstructural evaluation of the heat-affected zone in ultra-high strength steels, Thin-Walled Structures, 2020, 157, 107072.
[31] SSAB. Strenx Tube 960 MH. Data Sheet 2043, Sweden, 2017.
[32] EN 10219-2. Cold formed welded structural hollow sections of non-alloy and fine grain steels-Part 2: Tolerances, dimensions and sectional properties. European Committee for Standardization (CEN), Brussels, Belgium; 2006.
[33] EN 1993-1-1, Eurocode 3: Design of steel structures–Part 1-1: General rules and rules for buildings, European Committee for Standardization (CEN), Brussels, Belgium, 2005.
[34] AISI S100. North American Specification for the design of cold-formed steel structural members. American Iron and Steel Institute (AISI), Washington, D.C., USA, 2016.
[35] EN 1990. Eurocode: Basis of structural design. European Committee for Standardization (CEN), Brussels, Belgium, 2002.
[36] ASCE/SEI 7. Minimum Design Loads for Buildings and Other Structures. American Society of Civil Engineers (ASCE), New York, USA, 2016.
[37] Pandey, M. and Young, B., 2021. Post-fire mechanical response of high strength steels. Thin-Walled Structures, 164, p.107606.

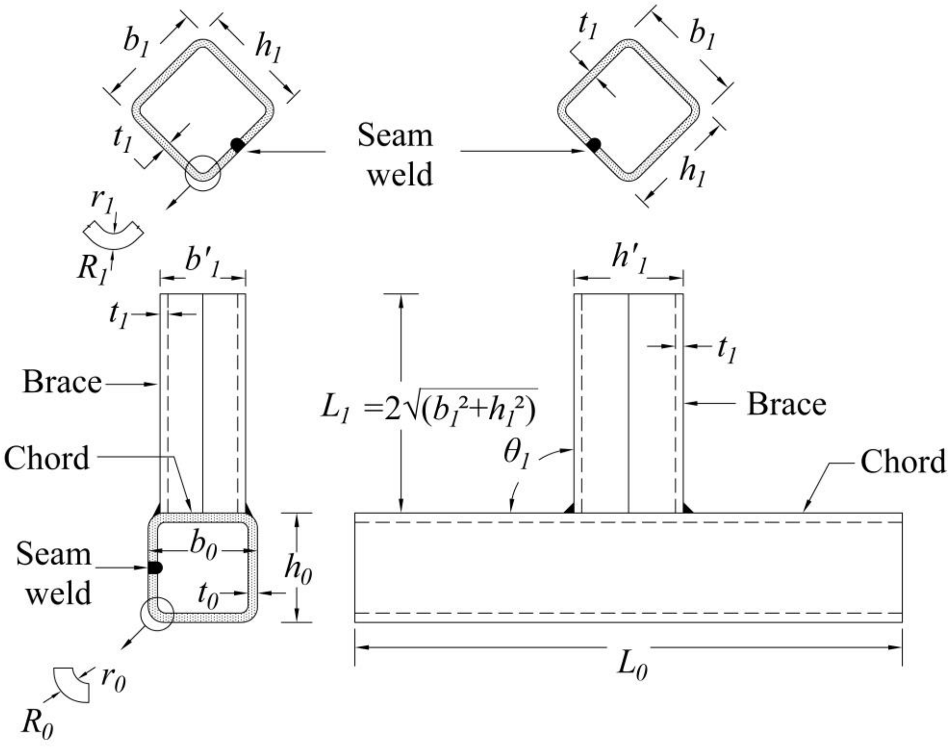

(a) Definitions of notations for BR T-joint (also valid for BR X-joint).

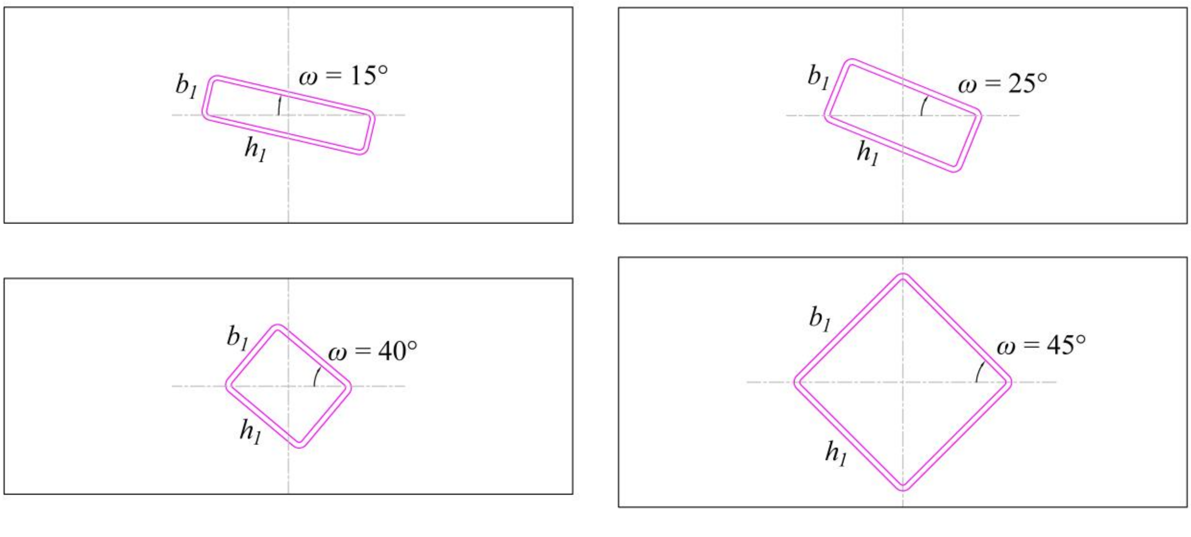

(b) Orientations of brace member adopted in the parametric study.

Fig. 1. Notations and brace rotation angles of BR T- and X-joints.

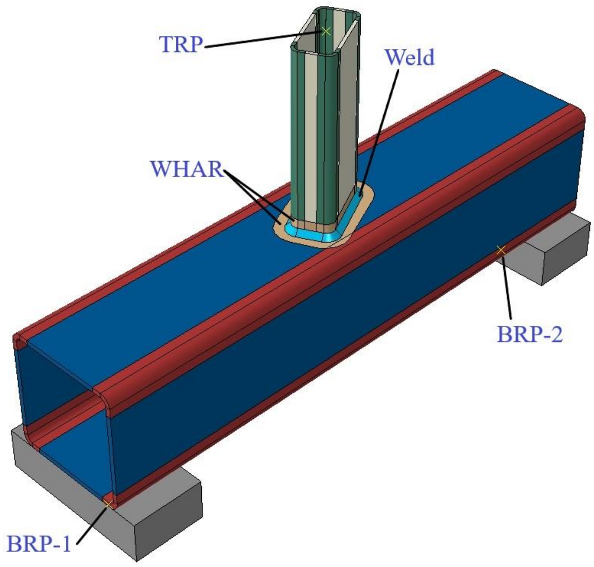

(a) BR T-joint FE model with ω = 27°.

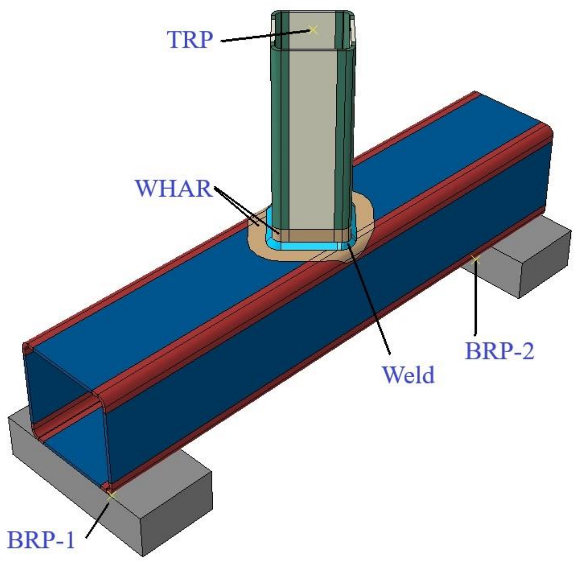

(b) BR T-joint FE model with ω = 45°.

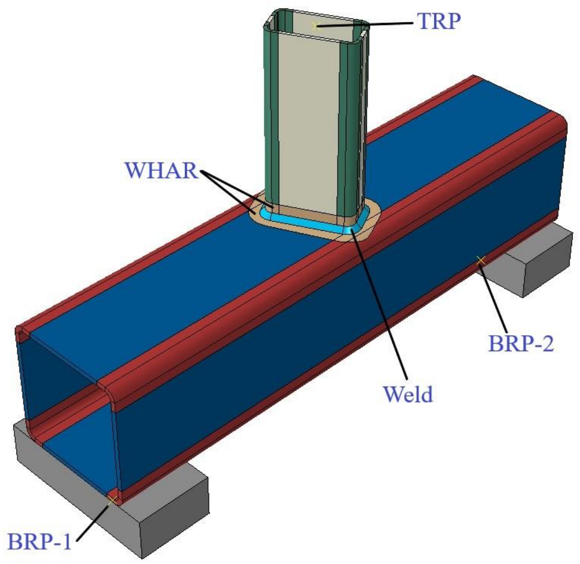

(c) BR T-joint FE model with ω = 63°.

Fig. 2. Typical FE models of BR T-joints.

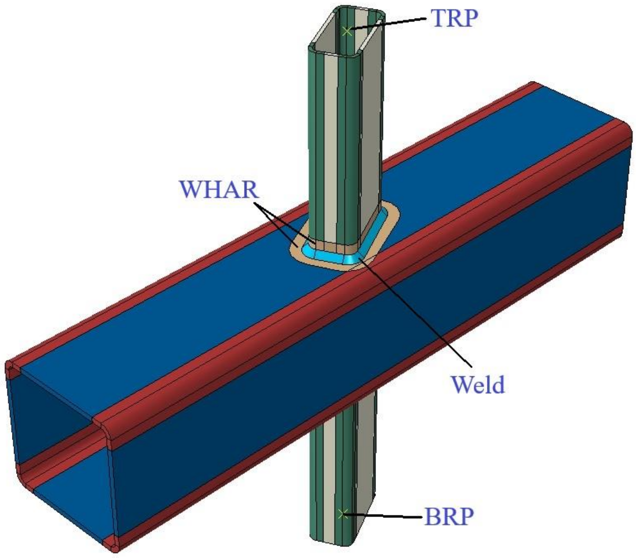

(a) BR X-joint FE model with ω = 27°.

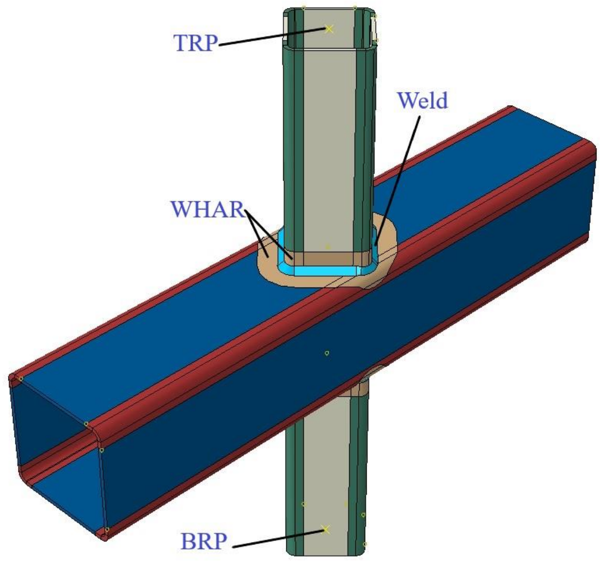

(b) BR X-joint FE model with ω = 45°.

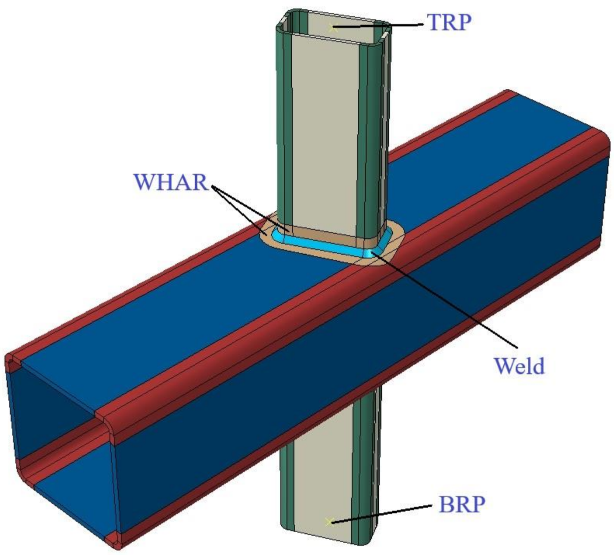

(c) BR X-joint FE model with ω = 63°.

Fig. 3. Typical FE models of BR X-joints.

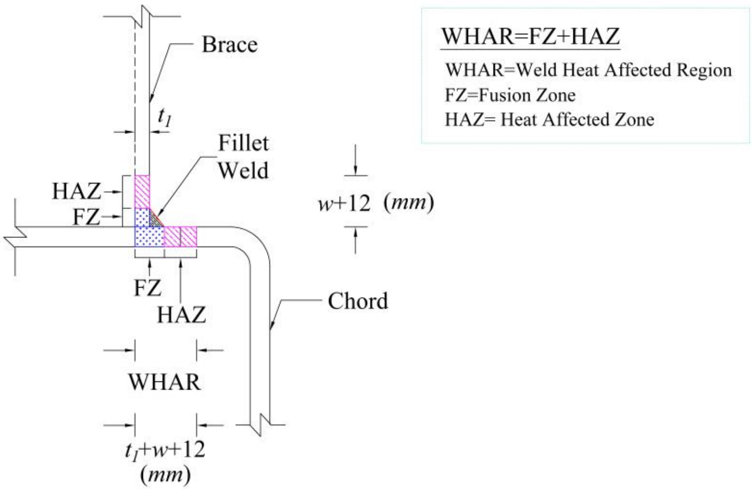

Fig. 4. Definition of weld heat affected region (WHAR) [15].

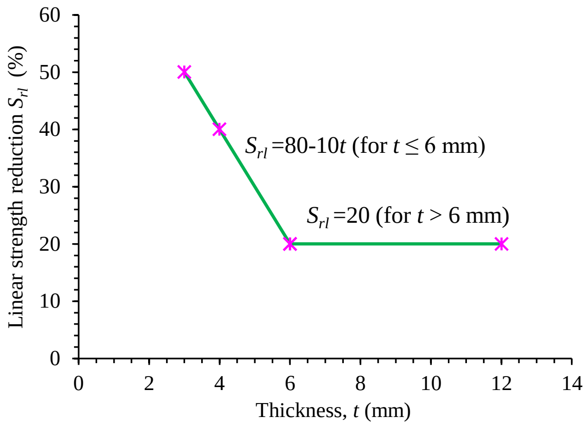

Fig. 5. Strength reduction model for WHAR of S900 and S960 steel grades tubular joints [15].

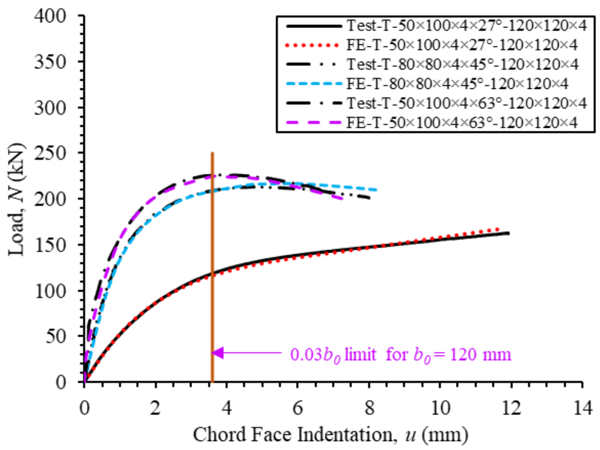

Fig. 6. Comparisons of test and FE load vs chord face indentation curves for BR T-joints.

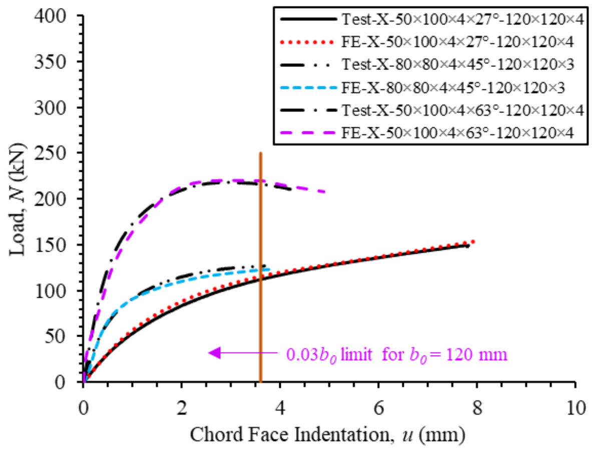

Fig. 7. Comparisons of test and FE load vs chord face indentation curves for BR X-joints.

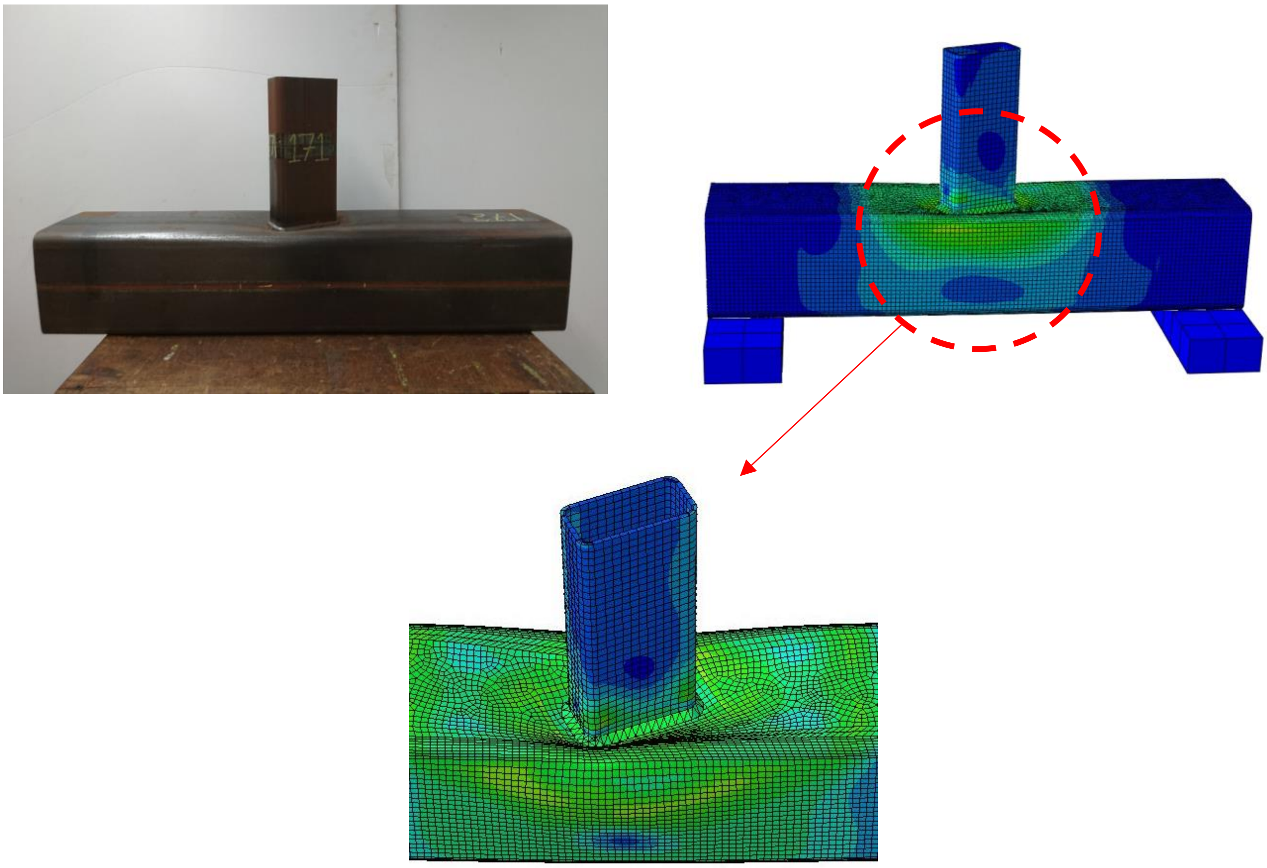

(a) Test vs FE comparison for chord face failure (F) mode of T-50×100×4×27°-150×150×6 ($\beta' = 0.55$).

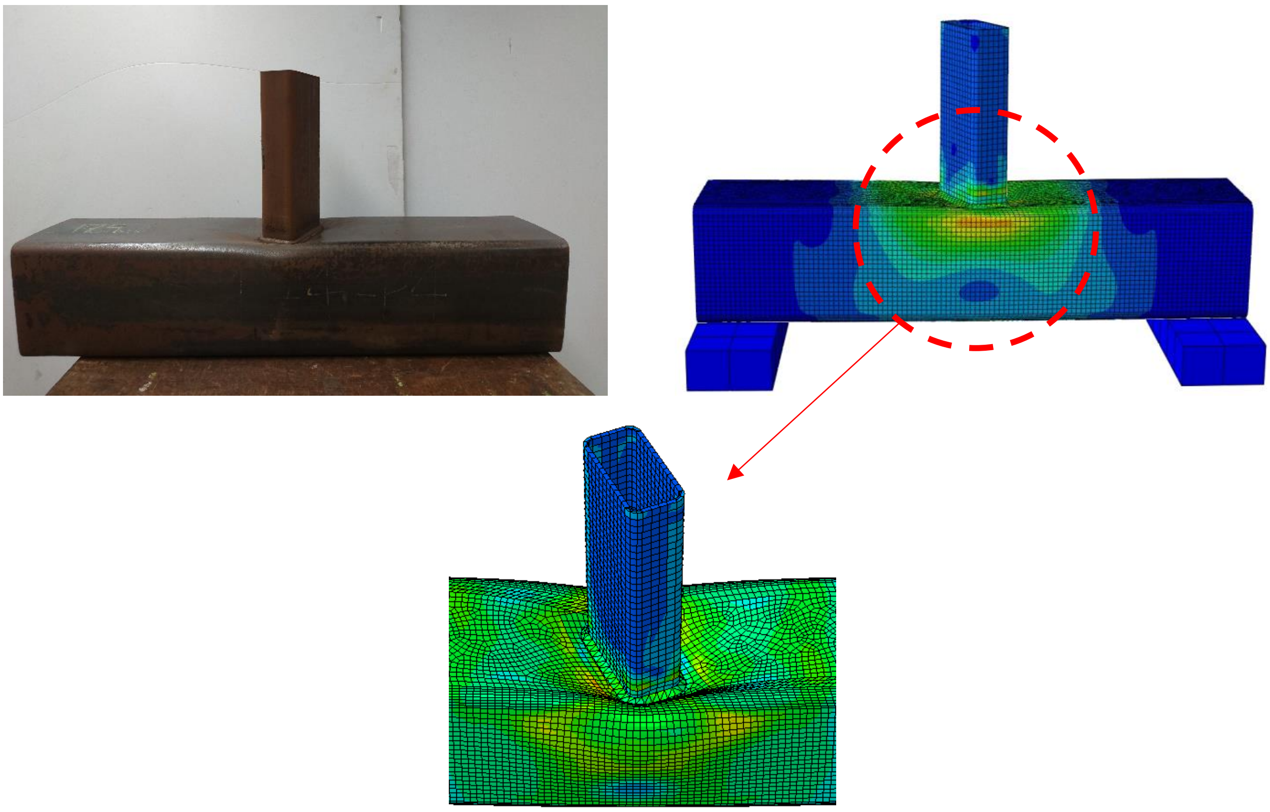

(b) Test vs FE comparison for chord face failure (F) mode of T-50×100×4×63°-150×150×6 ($\beta' = 0.70$).

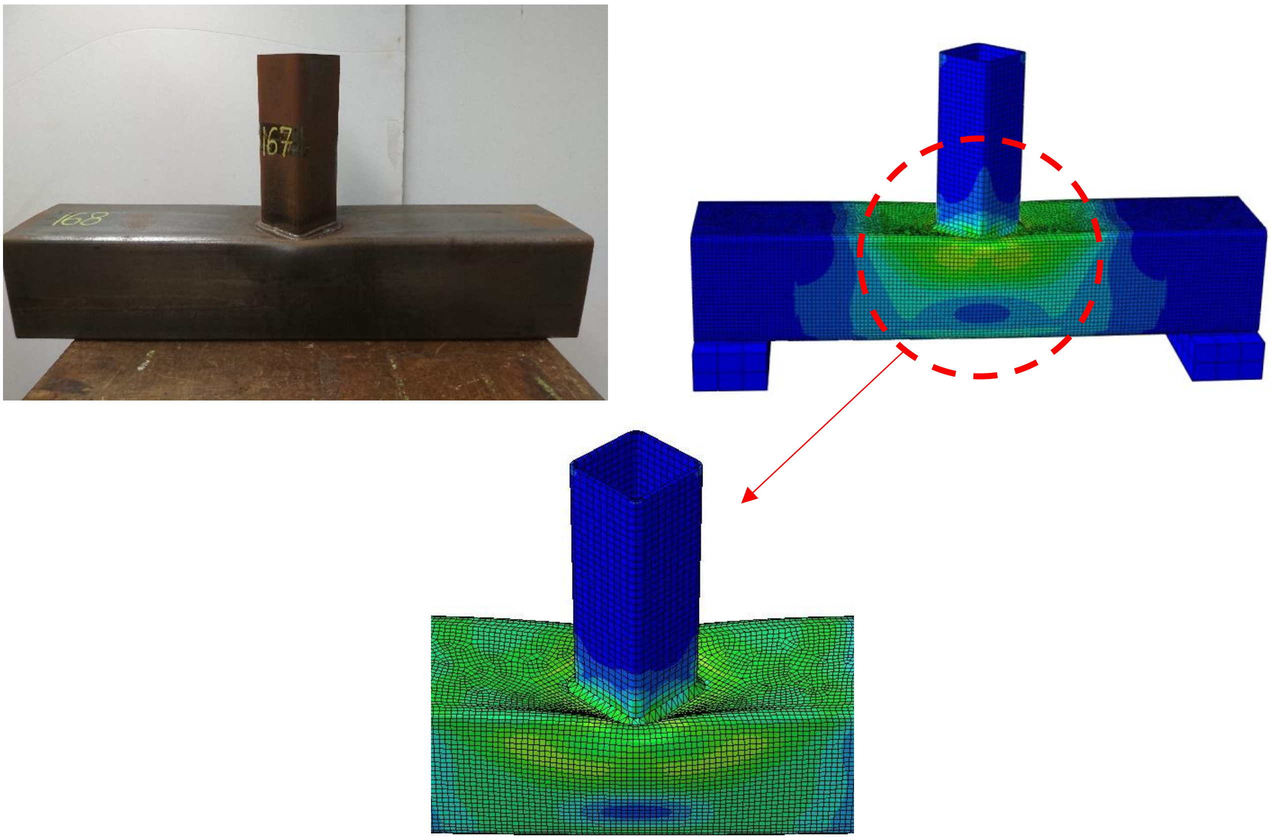

(c) Test vs FE comparison for combined failure (F+S) mode of T-80×80×4×45°-120×120×4 ($\beta' = 0.87$).

Fig. 8. Test vs FE failure modes comparisons for BR T-joints.

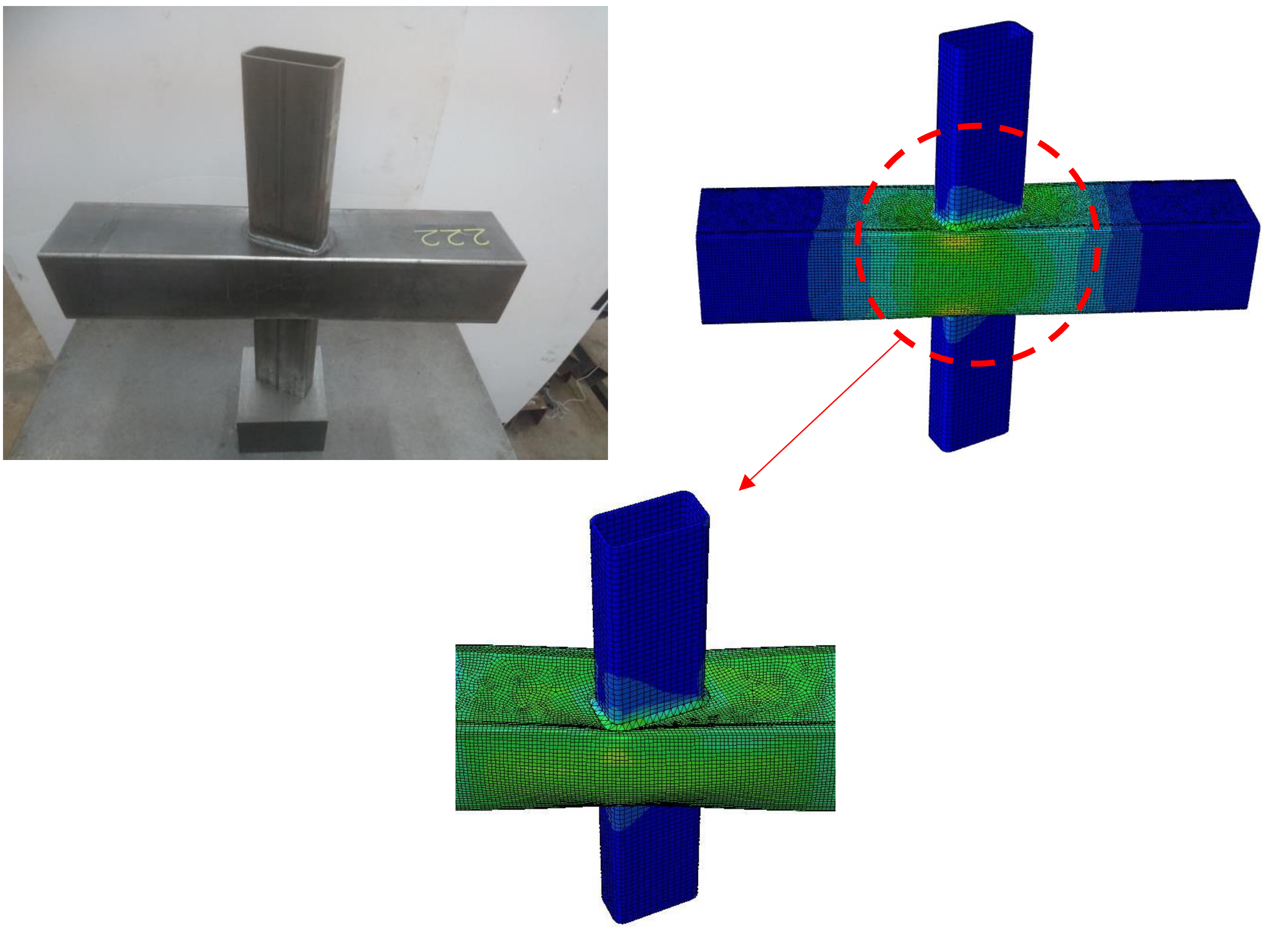

(a) Test vs FE comparison for chord face failure (F) mode of X-50×100×4×27°-120×120×3 ($\beta' = 0.68$).

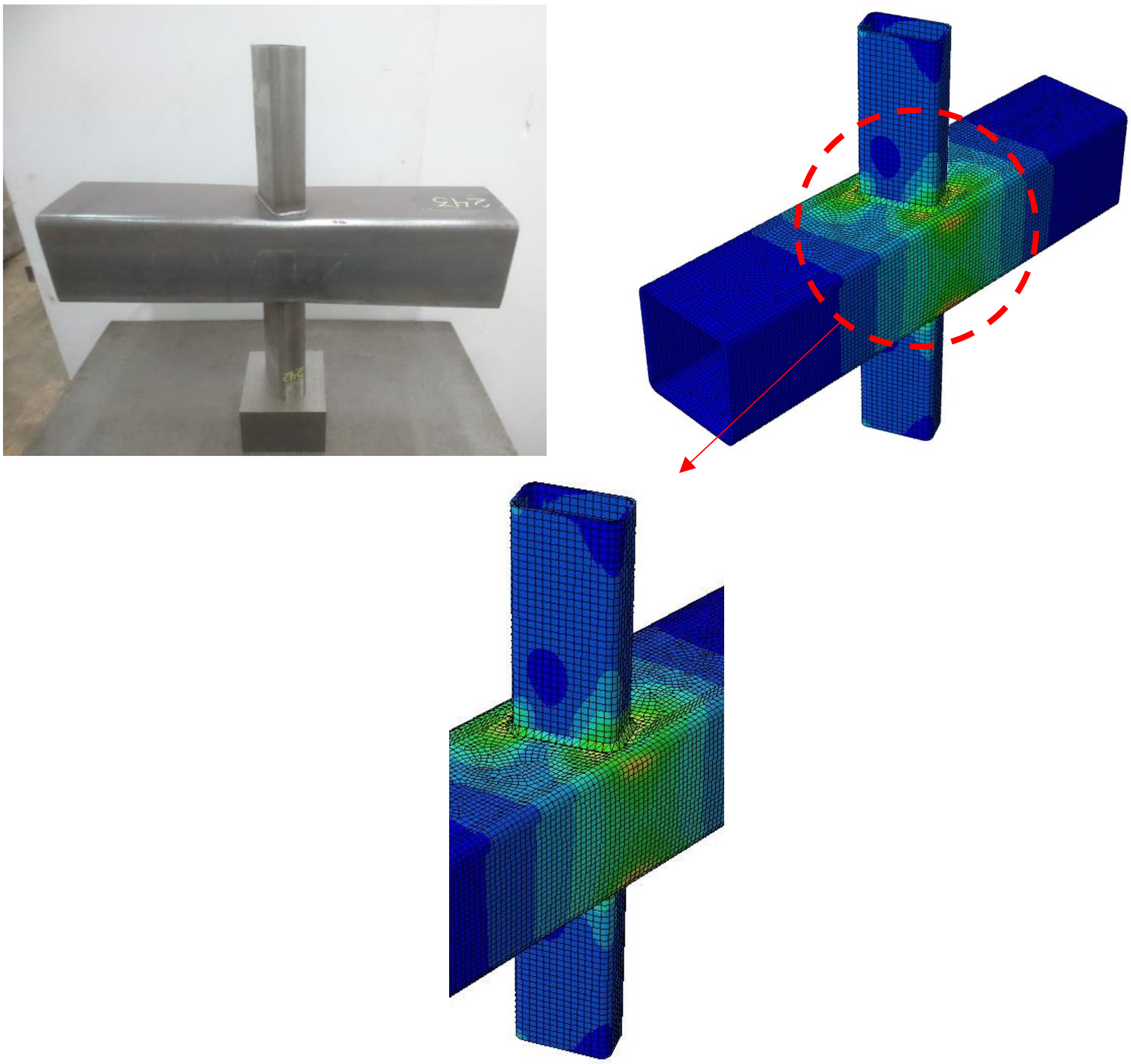

(b) Test vs FE comparison for chord face failure (F) mode of X-50×100×4×63°-150×150×6 ($\beta' = 0.70$).

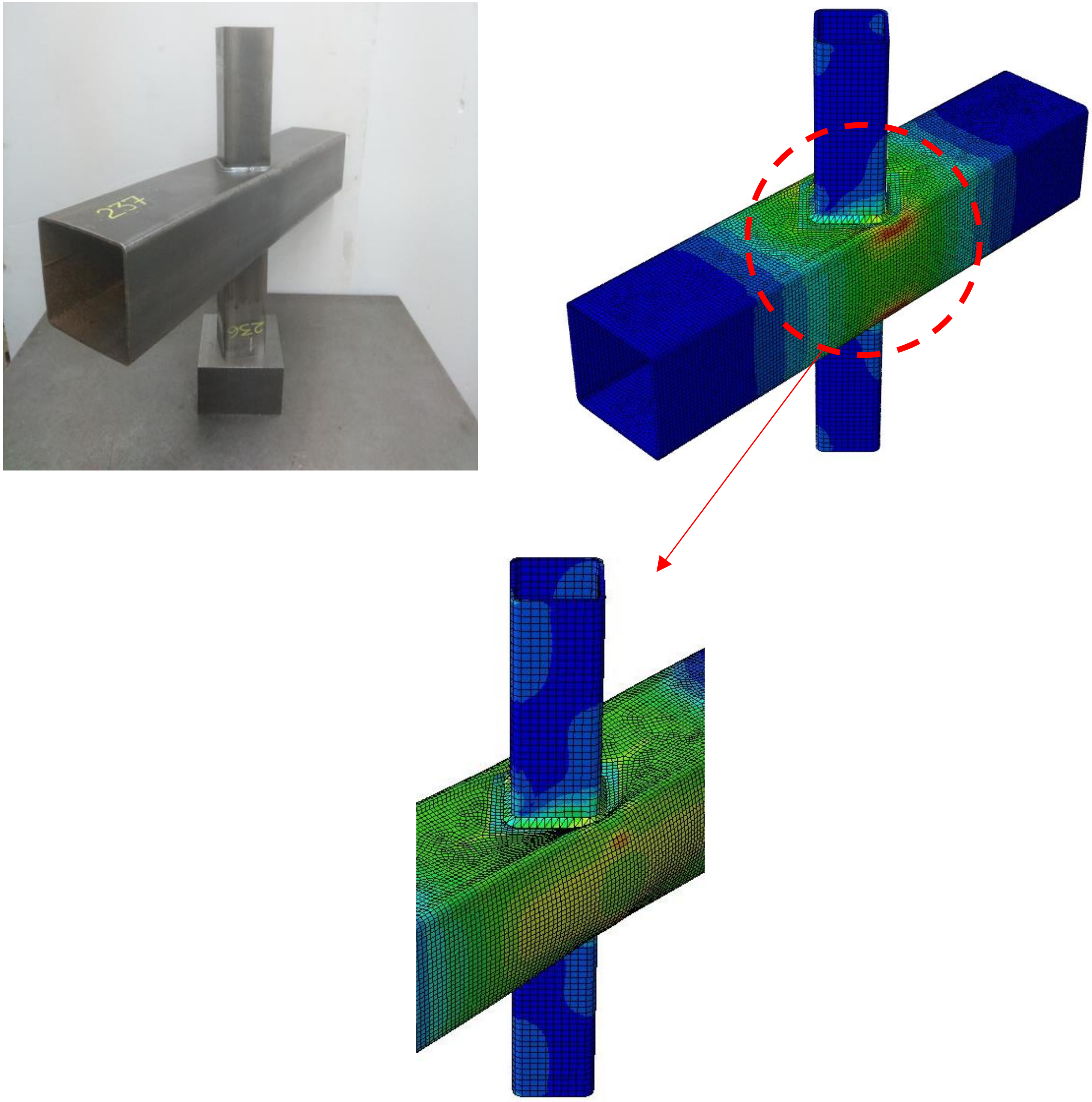

(c) Test vs FE comparison for combined failure (F+S) mode of X-80×80×4×45°-120×120×3 ($\beta' = 0.87$).

Fig. 9. Test vs FE failure modes comparisons for BR X-joints.

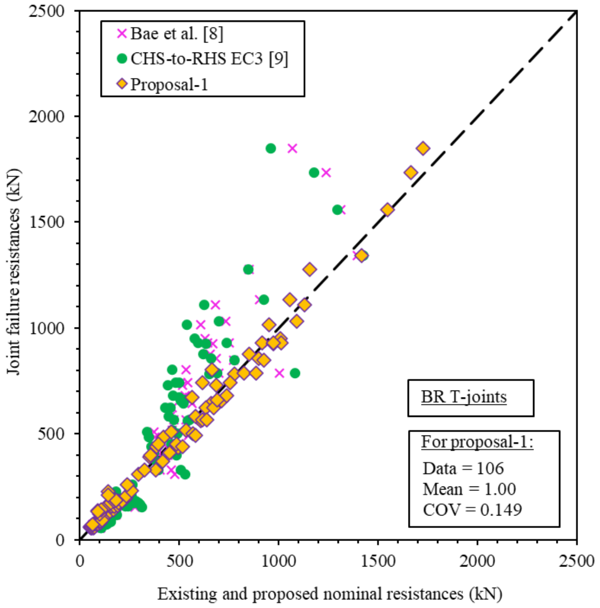

Fig. 10. Comparisons of test and FE joint failure resistances with existing and proposed (Proposal-1) nominal resistances for BR T-joints.

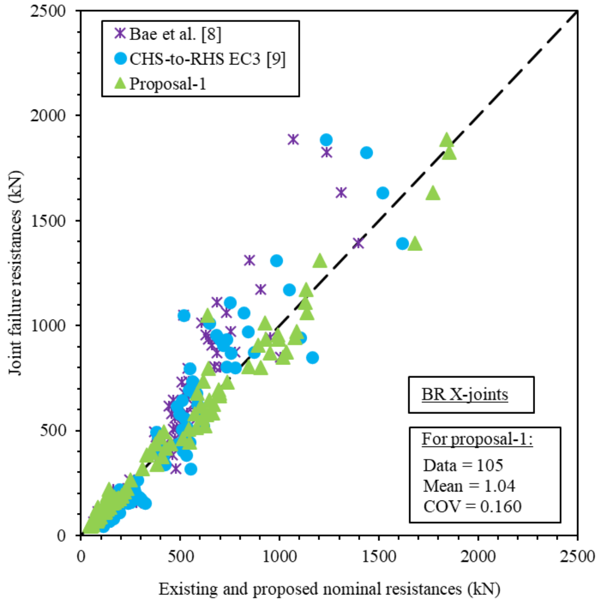

Fig. 11. Comparisons of test and FE joint failure resistances with existing and proposed (Proposal-1) nominal resistances for BR X-joints.

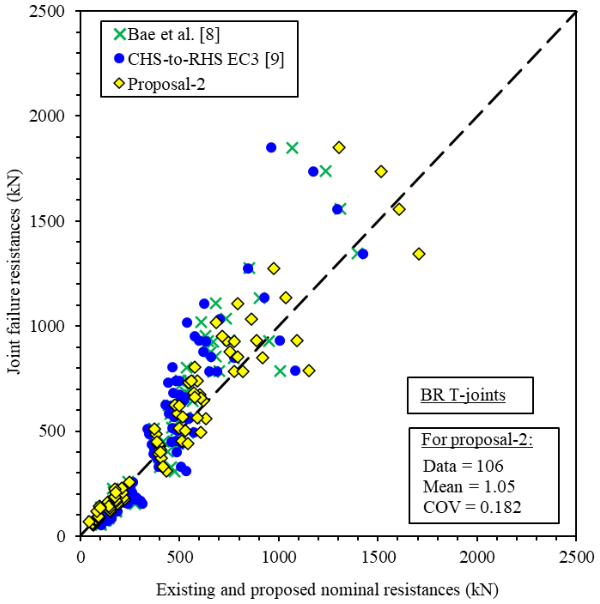

Fig. 12. Comparisons of test and FE joint failure resistances with existing and proposed (Proposal-2) nominal resistances for BR T-joints.

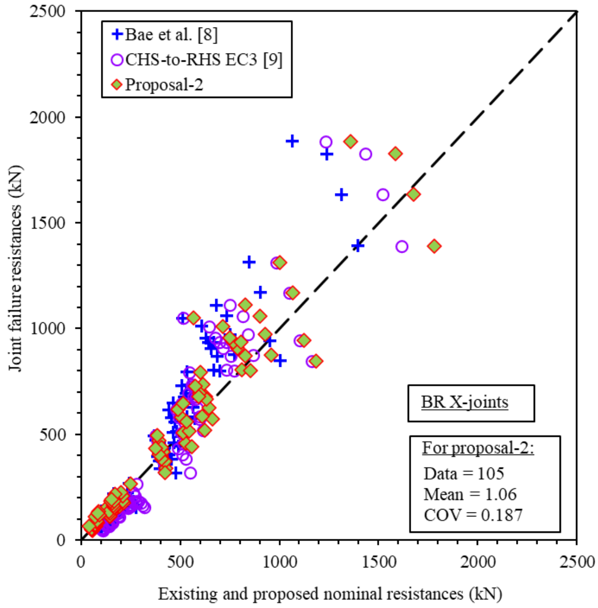

Fig. 13. Comparisons of test and FE joint failure resistances with existing and proposed (Proposal-2) nominal resistances for BR X-joints.

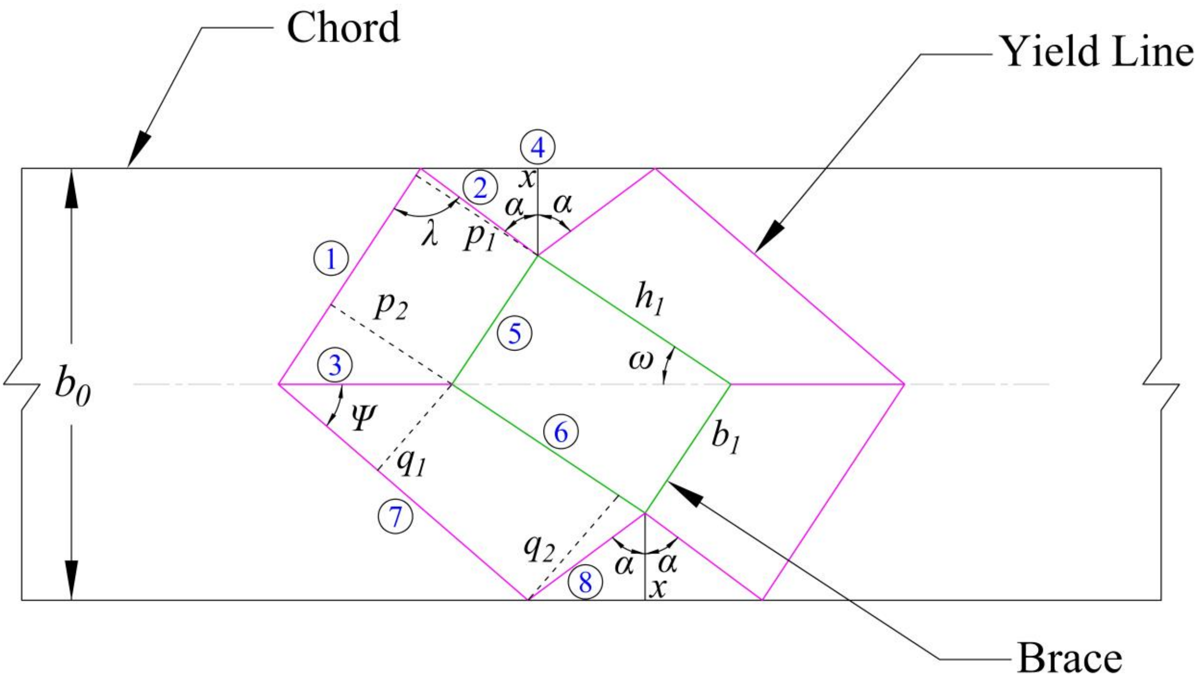

Fig. 14. Simplified yield line model of BR T- and X-joints.

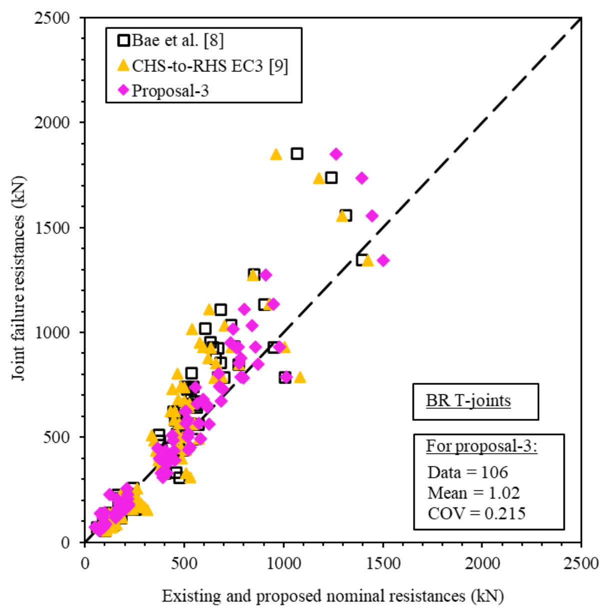

Fig. 15. Comparisons of test and FE joint failure resistances with existing and proposed (Proposal-3) nominal resistances for BR T-joints.

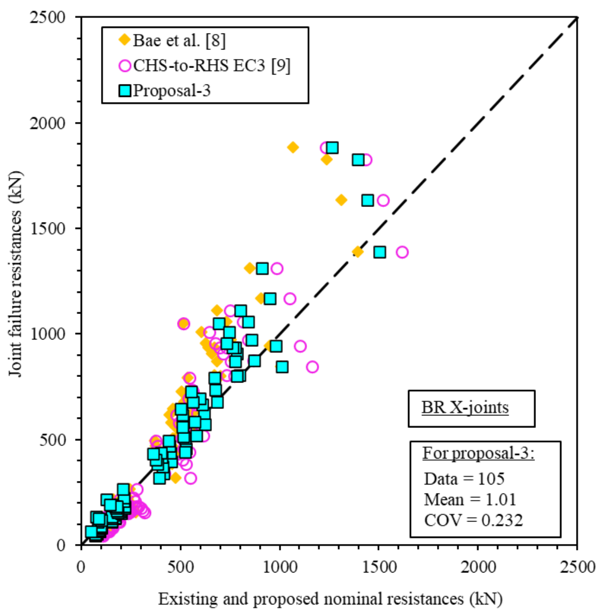

Fig. 16. Comparisons of test and FE joint failure resistances with existing and proposed (Proposal-3) nominal resistances for BR X-joints.

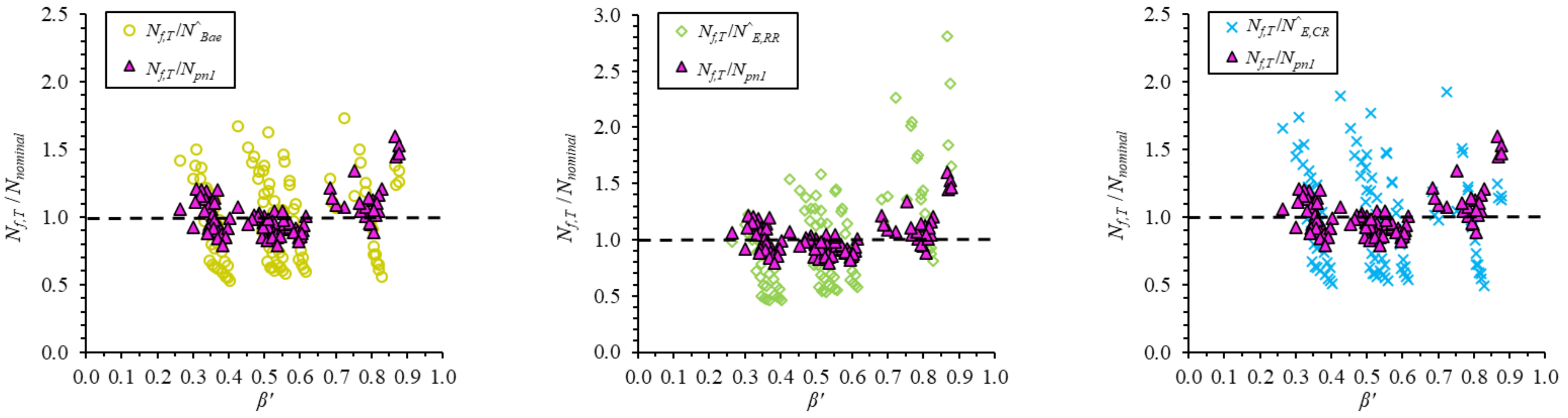

(a) For Bae et al. [8] (b) For RHS-to-RHS T-joint of EC3 [9] (c) For CHS-to-RHS T-joint of EC3 [9]

Fig. 17. Distributions of joint failure resistance ($N_{f,T}$) comparisons ratios for BR T-joints.

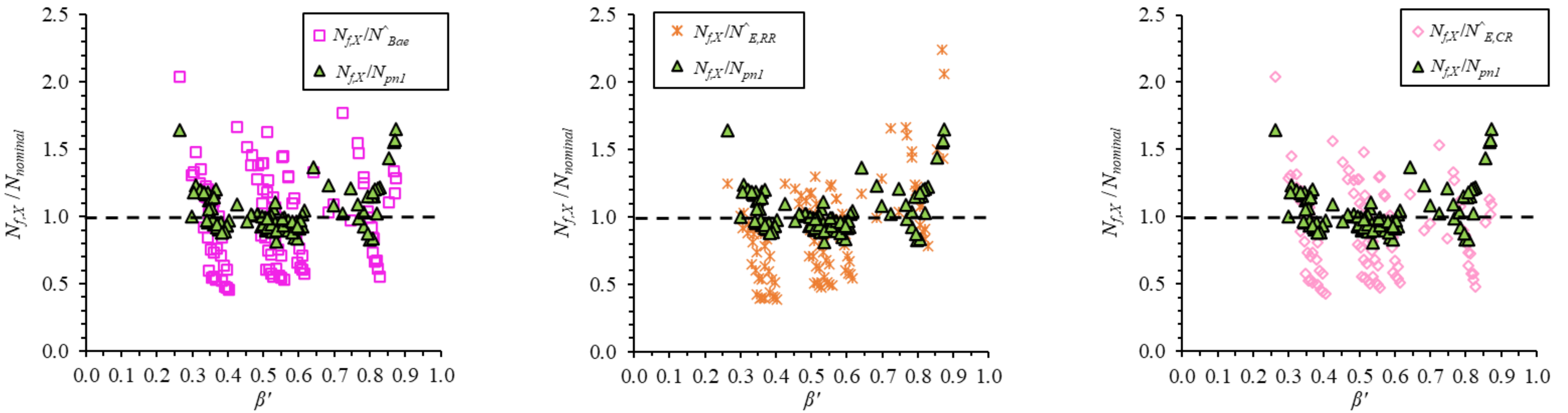

(a) For Bae et al. [8] (b) For RHS-to-RHS X-joint of EC3 [9] (c) For CHS-to-RHS X-joint of EC3 [9]

Fig. 18. Distributions of joint failure resistance ($N_{f,X}$) comparisons ratios for BR X-joints.

Table 1. Test vs FE resistance comparisons for BR T-joints.

Specimens	β'	Test Joint Failure Resistances (kN)#	Test Joint Ultimate Resistances (kN)#	Numerical Joint Failure Resistances (kN)	Numerical Joint Ultimate Resistances (kN)	Comparisons	
T-b_1×h_1×t_1× ω -b_0×h_0×t_0	$\frac{b_1'}{b_0}$	$N_{f,T}$	$N_{\max,T}$	$N_{f,FE}$	$N_{\max,FE}$	$\frac{N_{f,T}}{N_{f,FE}}$	$\frac{N_{\max,T}}{N_{\max,FE}}$
T-50×100×4×27°-150×150×6	0.55	185.7	-	186.2	-	1.00	-
T-50×100×4×27°-150×150×6-R	0.55	187.8	-	188.1	-	1.00	-
T-50×100×4×63°-150×150×6	0.70	258.1	-	257.8	-	1.00	-
T-50×100×4×27°-120×120×4	0.68	119.4	-	116.1	-	1.03	-
T-50×100×4×63°-120×120×4	0.87	226.2	226.50	223.9	224.1	1.01	1.01
T-50×100×4×27°-120×120×3	0.69	70.8	-	68.5	-	1.03	-
T-50×100×4×63°-120×120×3	0.88	137.9	138.40	137.2	138.71	1.01	1.00
T-80×80×4×45°-120×120×4	0.87	209.4	213.30	209.1	216.8	1.00	0.98
T-80×80×4×45°-140×140×4	0.75	142.0	-	138.1	-	1.03	-
T-80×80×4×45°-120×120×3	0.88	134.6	137.10	134.2	134.1	1.00	1.02
					Mean (P_m)	1.01	1.00
					COV (V_p)	0.014	0.017

Note: " - " denotes not applicable; #data obtained from Pandey and Young [1].

Table 2. Test vs FE resistance comparisons for BR X-joints.

Specimens	β'	Test Joint Failure Resistances (kN)[#]	Test Joint Ultimate Resistances (kN)[#]	Numerical Joint Failure Resistances (kN)	Numerical Joint Ultimate Resistances (kN)	Comparisons	
X-b_1×h_1×t_1× ω -b_0×h_0×t_0	$\frac{b_1'}{b_0}$	$N_{f,X}$	$N_{\max,X}$	$N_{f,FE}$	$N_{\max,FE}$	$\frac{N_{f,X}}{N_{f,FE}}$	$\frac{N_{\max,X}}{N_{\max,FE}}$
X-50×100×4×27°-150×150×6	0.53	184.4	-	182.5	-	1.01	-
X-50×100×4×63°-150×150×6	0.70	266.9	-	265.7	-	1.00	-
X-50×100×4×27°-120×120×4	0.64	112.8	-	115.6	-	0.98	-
X-50×100×4×63°-120×120×4	0.87	218.4	218.4	219.5	219.9	0.99	0.99
X-50×100×4×27°-120×120×3	0.68	64.9	-	65.0	-	1.00	-
X-50×100×4×63°-120×120×3	0.87	136.3	136.3	136.0	136.10	1.00	1.00
X-80×80×4×45°-120×120×4	0.85	191.7	197.6	182.5	190.70	1.05	1.04
X-80×80×4×45°-140×140×4	0.75	120.1	-	116.1	-	1.03	-
X-80×80×4×45°-120×120×3	0.87	126.5	127.0	122.9	123.3	1.03	1.03
					Mean (P_m)	1.01	1.02
					COV (V_p)	0.023	0.021

Note: " - " denotes not applicable; [#]data obtained from Pandey and Young [2].

Table 3. Ranges of critical parameters used in parametric study.

Parameters	Validity Ranges
β (b_1/b_0)	[0.20 to 0.67]
β' (b_1'/b_0)	[0.26 to 0.88]
2γ (b_0/t_0)	[16.6 to 40]
τ (t_1/t_0)	[0.50 to 1.28]
ω	[15° to 63°]
θ_1	90°

Table 4. Mechanical properties of tubular member and weld adopted in parametric study.

Materials	Measured Mechanical Properties						
	E (GPa)	$\sigma_{0.2}$ (MPa)	$\varepsilon_{0.2}$ (%)	σ_u (MPa)	ε_u (%)	ε_f (%)	n
SHS/RHS (150×150×6) [11]	208.5	1059.1	0.71	1145.7	1.48	9.37[a]	5.31
Weld Material [12]	202.7	965.2	0.68	1023.4	5.41	17.15[b]	8.13

Note: [a] fracture strain based on 50 mm gauge length; [b] fracture strain based on 25 mm gauge length.

Table 5. Comparisons between test and FE resistances with existing and proposed nominal resistances for BR T-joints.

Specimens	β'	Joint Failure Resistances (kN)	Comparisons					
T-b_1×h_1×t_1× ω -b_0×h_0×t_0	$\frac{b_1'}{b_0}$	$N_{f,T}$	$\frac{N_{f,T}}{\hat{N}_{Bae}}$	$\frac{N_{f,T}}{\hat{N}_{E,RR}}$	$\frac{N_{f,T}}{\hat{N}_{E,CR}}$	$\frac{N_{f,T}}{N_{pn1}}$	$\frac{N_{f,T}}{N_{pn2}}$	$\frac{N_{f,T}}{N_{pn3}}$
T-40×150×6×15°-200×200×12	0.34	671.9	1.22	0.99	1.34	1.19	1.12	0.98
T-40×150×7.8×15°-200×200×12	0.32	740.7	1.36	1.11	1.54	1.20	1.26	1.09
T-40×150×9.6×15°-200×200×12	0.31	804.0	1.50	1.22	1.74	1.21	1.39	1.20
T-60×150×12×15°-200×200×12	0.26	730.2	1.42	0.99	1.66	1.06	1.34	1.05
T-40×150×5×15°-200×200×10	0.35	390.2	1.01	0.79	1.06	1.10	0.99	0.86
T-40×150×6.5×15°-200×200×10	0.33	438.0	1.15	0.90	1.22	1.13	1.13	0.97
T-40×150×8×15°-200×200×10	0.32	484.5	1.29	1.00	1.39	1.15	1.27	1.09
T-40×150×10×15°-200×200×10	0.31	510.9	1.38	1.06	1.51	1.11	1.37	1.16
T-40×150×3.33×15°-200×200×6.66	0.36	134.1	0.77	0.58	0.77	1.14	0.94	0.78
T-40×150×4.33×15°-200×200×6.66	0.35	137.9	0.80	0.60	0.80	1.06	0.97	0.81
T-40×150×5.33×15°-200×200×6.66	0.34	152.5	0.89	0.67	0.90	1.07	1.09	0.90
T-40×150×6.66×15°-200×200×6.66	0.33	164.3	0.97	0.72	0.99	1.04	1.19	0.98
T-40×150×2.5×15°-200×200×5	0.37	61.1	0.62	0.46	0.61	1.20	1.01	0.78
T-40×150×3.25×15°-200×200×5	0.36	62.3	0.64	0.47	0.62	1.10	1.03	0.80
T-40×150×4×15°-200×200×5	0.36	62.9	0.65	0.48	0.63	1.01	1.05	0.81
T-40×150×5×15°-200×200×5	0.35	65.4	0.68	0.50	0.67	0.94	1.11	0.85
T-60×60×6×45°-200×200×12	0.37	561.3	0.98	0.91	1.03	0.93	0.89	0.90
T-60×60×7.8×45°-200×200×12	0.36	643.6	1.14	1.06	1.23	0.97	1.04	1.04
T-60×60×9.6×45°-200×200×12	0.34	656.6	1.18	1.09	1.29	0.92	1.08	1.07

T-60×60×12×45°-200×200×12	0.30	682.5	1.28	1.14	1.45	0.92	1.20	1.14
T-60×60×5×45°-200×200×10	0.38	329.6	0.82	0.74	0.83	0.87	0.79	0.80
T-60×60×6.5×45°-200×200×10	0.37	371.8	0.94	0.84	0.97	0.89	0.91	0.91
T-60×60×8×45°-200×200×10	0.36	412.7	1.06	0.94	1.10	0.91	1.03	1.01
T-60×60×10×45°-200×200×10	0.34	437.0	1.14	1.01	1.20	0.88	1.11	1.08
T-60×60×3.33×45°-200×200×6.66	0.40	116.0	0.64	0.56	0.62	0.92	0.77	0.74
T-60×60×4.33×45°-200×200×6.66	0.39	120.8	0.67	0.59	0.66	0.87	0.81	0.78
T-60×60×5.33×45°-200×200×6.66	0.38	132.7	0.75	0.65	0.74	0.87	0.90	0.86
T-60×60×6.66×45°-200×200×6.66	0.37	142.1	0.81	0.70	0.80	0.84	0.98	0.93
T-60×60×2.5×45°-200×200×5	0.40	54.2	0.53	0.46	0.51	0.99	0.85	0.76
T-60×60×3.25×45°-200×200×5	0.40	55.9	0.55	0.48	0.53	0.92	0.88	0.79
T-60×60×4×45°-200×200×5	0.39	56.9	0.56	0.49	0.54	0.85	0.91	0.80
T-60×60×5×45°-200×200×5	0.38	59.0	0.59	0.50	0.57	0.79	0.95	0.84
T-60×130×6×25°-200×200×12	0.50	783.6	1.17	1.12	1.20	1.01	1.01	0.98
T-60×130×7.8×25°-200×200×12	0.48	877.2	1.34	1.28	1.41	1.03	1.16	1.12
T-60×130×9.6×25°-200×200×12	0.47	930.1	1.45	1.38	1.56	1.02	1.26	1.20
T-60×130×12×25°-200×200×12	0.42	1017.2	1.68	1.54	1.89	1.07	1.49	1.37
T-60×130×5×25°-200×200×10	0.51	452.7	0.96	0.88	0.94	0.93	0.88	0.86
T-60×130×6.5×25°-200×200×10	0.50	516.0	1.11	1.02	1.11	0.96	1.03	0.99
T-60×130×8×25°-200×200×10	0.48	582.4	1.28	1.17	1.30	1.00	1.19	1.13
T-60×130×10×25°-200×200×10	0.47	624.1	1.40	1.26	1.45	0.98	1.31	1.23
T-60×130×3.33×25°-200×200×6.66	0.52	158.1	0.74	0.66	0.69	0.98	0.85	0.79
T-60×130×4.33×25°-200×200×6.66	0.51	163.7	0.77	0.68	0.73	0.91	0.89	0.82
T-60×130×5.33×25°-200×200×6.66	0.51	183.9	0.88	0.77	0.84	0.94	1.02	0.93
T-60×130×6.66×25°-200×200×6.66	0.49	184.4	0.90	0.78	0.86	0.85	1.04	0.94
T-60×130×2.5×25°-200×200×5	0.53	73.7	0.61	0.54	0.56	1.05	0.93	0.80
T-60×130×3.25×25°-200×200×5	0.52	75.7	0.63	0.55	0.58	0.97	0.97	0.83
T-60×130×4×25°-200×200×5	0.52	74.4	0.62	0.54	0.58	0.87	0.96	0.82
T-60×130×5×25°-200×200×5	0.51	79.1	0.67	0.58	0.63	0.83	1.04	0.88
T-75×90×6×40°-200×200×12	0.53	786.0	1.12	1.14	1.14	0.95	0.96	1.00
T-75×90×7.8×40°-200×200×12	0.51	854.4	1.25	1.26	1.29	0.95	1.08	1.10
T-75×90×9.6×40°-200×200×12	0.50	925.7	1.38	1.39	1.46	0.95	1.20	1.21
T-75×90×12×40°-200×200×12	0.45	951.9	1.51	1.44	1.65	0.95	1.33	1.30
T-75×90×5×40°-200×200×10	0.54	439.0	0.89	0.87	0.86	0.85	0.81	0.84
T-75×90×6.5×40°-200×200×10	0.52	502.9	1.04	1.01	1.02	0.89	0.95	0.97
T-75×90×8×40°-200×200×10	0.51	566.8	1.19	1.15	1.19	0.92	1.10	1.11
T-75×90×10×40°-200×200×10	0.50	622.2	1.34	1.28	1.37	0.92	1.24	1.24
T-75×90×3.33×40°-200×200×6.66	0.55	156.6	0.70	0.67	0.65	0.91	0.80	0.79
T-75×90×4.33×40°-200×200×6.66	0.54	163.4	0.74	0.70	0.69	0.86	0.84	0.83
T-75×90×5.33×40°-200×200×6.66	0.53	181.4	0.83	0.78	0.78	0.87	0.95	0.93
T-75×90×6.66×40°-200×200×6.66	0.52	196.0	0.91	0.84	0.86	0.85	1.05	1.02
T-75×90×2.5×40°-200×200×5	0.56	74.2	0.58	0.55	0.53	0.99	0.89	0.81
T-75×90×3.25×40°-200×200×5	0.55	75.8	0.60	0.56	0.55	0.91	0.92	0.84
T-75×90×4×40°-200×200×5	0.55	77.9	0.62	0.58	0.57	0.86	0.95	0.87
T-75×90×5×40°-200×200×5	0.54	80.3	0.65	0.60	0.60	0.79	1.00	0.90
T-90×90×6×45°-200×200×12	0.59	847.6	1.10	1.14	1.09	0.92	0.92	0.97
T-90×90×7.8×45°-200×200×12	0.57	931.6	1.24	1.27	1.26	0.92	1.05	1.09
T-90×90×9.6×45°-200×200×12	0.56	1033.3	1.41	1.45	1.47	0.95	1.20	1.23
T-90×90×12×45°-200×200×12	0.51	1108.6	1.62	1.58	1.77	0.98	1.40	1.38
T-90×90×5×45°-200×200×10	0.59	492.6	0.90	0.90	0.86	0.85	0.81	0.85
T-90×90×6.5×45°-200×200×10	0.58	565.1	1.06	1.05	1.03	0.89	0.96	0.99
T-90×90×8×45°-200×200×10	0.57	660.6	1.27	1.25	1.25	0.96	1.15	1.17
T-90×90×10×45°-200×200×10	0.55	740.0	1.46	1.43	1.48	0.98	1.33	1.34
T-90×90×3.33×45°-200×200×6.66	0.61	173.4	0.70	0.68	0.64	0.90	0.78	0.78
T-90×90×4.33×45°-200×200×6.66	0.60	183.5	0.75	0.72	0.69	0.86	0.84	0.84
T-90×90×5.33×45°-200×200×6.66	0.59	208.0	0.86	0.83	0.80	0.89	0.97	0.96
T-90×90×6.66×45°-200×200×6.66	0.58	229.5	0.97	0.92	0.91	0.89	1.10	1.07
T-90×90×2.5×45°-200×200×5	0.62	84.1	0.59	0.58	0.53	1.00	0.89	0.83
T-90×90×3.25×45°-200×200×5	0.61	87.2	0.62	0.60	0.56	0.94	0.93	0.86

T-90×90×4×45°-200×200×5	0.60	89.7	0.65	0.62	0.59	0.88	0.97	0.89
T-90×90×5×45°-200×200×5	0.59	93.1	0.68	0.64	0.62	0.82	1.03	0.94
T-120×120×6×45°-200×200×12	0.80	1344.2	0.96	1.44	0.94	0.95	0.79	0.90
T-120×120×7.8×45°-200×200×12	0.78	1557.5	1.19	1.75	1.20	1.01	0.97	1.08
T-120×120×9.6×45°-200×200×12	0.77	1736.4	1.40	2.05	1.48	1.04	1.15	1.25
T-120×120×12×45°-200×200×12	0.72	1850.0	1.73	2.26	1.93	1.07	1.42	1.47
T-120×120×5×45°-200×200×10	0.81	787.3	0.78	1.12	0.73	0.89	0.68	0.78
T-120×120×6.5×45°-200×200×10	0.79	929.5	0.98	1.36	0.92	0.96	0.85	0.95
T-120×120×8×45°-200×200×10	0.78	1133.7	1.25	1.73	1.22	1.08	1.09	1.20
T-120×120×10×45°-200×200×10	0.77	1275.5	1.50	2.01	1.51	1.10	1.31	1.40
T-120×120×3.33×45°-200×200×6.66	0.82	308.3	0.65	0.93	0.58	1.05	0.71	0.78
T-120×120×4.33×45°-200×200×6.66	0.81	330.0	0.72	1.00	0.65	1.01	0.79	0.86
T-120×120×5.33×45°-200×200×6.66	0.80	400.5	0.91	1.23	0.82	1.12	0.99	1.07
T-120×120×6.66×45°-200×200×6.66	0.79	450.1	1.07	1.40	0.98	1.14	1.17	1.24
T-120×120×2.5×45°-200×200×5	0.83	154.3	0.56	0.81	0.49	1.21	0.82	0.84
T-120×120×3.25×45°-200×200×5	0.82	165.2	0.61	0.87	0.54	1.16	0.90	0.92
T-120×120×4×45°-200×200×5	0.82	172.4	0.66	0.91	0.59	1.11	0.97	0.98
T-120×120×5×45°-200×200×5	0.81	182.5	0.73	0.97	0.65	1.05	1.06	1.06
T-50×100×4×27°-150×150×6	0.55	185.7*	1.04	0.97	0.99	1.03	1.06	1.01
T-50×100×4×27°-150×150×6-R	0.55	187.8*	1.05	0.97	1.00	1.04	1.07	1.02
T-50×100×4×63°-150×150×6	0.70	258.1*	1.07	1.38	0.98	1.09	1.05	1.23
T-50×100×4×27°-120×120×4	0.68	119.4*	1.28	1.36	1.19	1.22	1.45	1.35
T-50×100×4×63°-120×120×4	0.87	226.2*	1.38	2.81	1.24	1.60	1.31	1.80
T-50×100×4×27°-120×120×3	0.69	70.8*	1.11	1.16	1.01	1.14	1.57	1.38
T-50×100×4×63°-120×120×3	0.88	137.9*	1.34	2.39	1.16	1.53	1.39	1.84
T-80×80×4×45°-120×120×4	0.87	209.4*	1.24	1.84	1.14	1.45	1.16	1.33
T-80×80×4×45°-140×140×4	0.75	142.0*	1.15	1.36	1.05	1.34	1.45	1.44
T-80×80×4×45°-120×120×3	0.88	134.6*	1.26	1.66	1.12	1.47	1.33	1.45
		Mean (P_m)	0.99	1.02	0.99	1.00	1.05	1.02
		COV (V_p)	0.311	0.437	0.365	0.149	0.182	0.215
		Resistance factor (ϕ)	1.00	1.00	1.00	0.80	0.80	0.70
		Reliability index (β_0)	1.25	0.96	1.04	2.52	2.51	2.66

Note: * data obtained from Pandey and Young [1].

Table 6. Comparisons between test and FE resistances with existing and proposed nominal resistances for BR X-joints.

Specimens	β'	Joint Failure Resistances (kN)	Comparisons					
X-b_1×h_1×t_1× ω -b_0×h_0×t_0	$\frac{b_1'}{b_0}$	$N_{f,X}$	$\frac{N_{f,X}}{\hat{N}_{Bae}}$	$\frac{N_{f,X}}{\hat{N}_{E,RR}}$	$\frac{N_{f,X}}{\hat{N}_{E,CR}}$	$\frac{N_{f,X}}{N_{pn1}}$	$\frac{N_{f,X}}{N_{pn2}}$	$\frac{N_{f,X}}{N_{pn3}}$
X-40×150×6×15°-200×200×12	0.34	677.8	1.23	0.88	1.19	1.16	1.08	0.99
X-40×150×7.8×15°-200×200×12	0.32	734.9	1.35	0.95	1.32	1.20	1.19	1.09
X-40×150×9.6×15°-200×200×12	0.31	794.4	1.48	1.03	1.45	1.24	1.32	1.18
X-60×150×12×15°-200×200×12	0.26	1050.4	2.04	1.24	2.04	1.64	1.85	1.52
X-40×150×5×15°-200×200×10	0.35	395.7	1.02	0.74	0.99	1.12	0.97	0.87
X-40×150×6.5×15°-200×200×10	0.33	437.9	1.15	0.81	1.11	1.17	1.09	0.97
X-40×150×8×15°-200×200×10	0.32	471.0	1.25	0.88	1.22	1.20	1.20	1.06
X-40×150×10×15°-200×200×10	0.31	493.6	1.33	0.92	1.31	1.18	1.28	1.12
X-40×150×3.33×15°-200×200×6.66	0.36	127.4	0.73	0.53	0.70	1.18	0.91	0.74
X-40×150×4.33×15°-200×200×6.66	0.35	130.8	0.76	0.55	0.73	1.13	0.95	0.77
X-40×150×5.33×15°-200×200×6.66	0.34	144.9	0.85	0.61	0.82	1.18	1.06	0.86
X-40×150×6.66×15°-200×200×6.66	0.33	155.6	0.92	0.65	0.89	1.18	1.16	0.93
X-40×150×2.5×15°-200×200×5	0.37	52.7	0.53	0.39	0.51	1.20	0.98	0.67

X-40×150×3.25×15°-200×200×5	0.36	53.9	0.55	0.40	0.53	1.14	1.02	0.69
X-40×150×4×15°-200×200×5	0.36	53.4	0.55	0.40	0.53	1.06	1.01	0.69
X-40×150×5×15°-200×200×5	0.35	57.5	0.59	0.43	0.57	1.06	1.11	0.74
X-60×60×6×45°-200×200×12	0.37	574.8	1.00	0.84	0.96	0.91	0.87	0.92
X-60×60×7.8×45°-200×200×12	0.36	626.3	1.11	0.91	1.07	0.94	0.97	1.01
X-60×60×9.6×45°-200×200×12	0.34	667.2	1.20	0.97	1.16	0.96	1.05	1.09
X-60×60×12×45°-200×200×12	0.30	694.2	1.31	1.01	1.29	1.00	1.16	1.16
X-60×60×5×45°-200×200×10	0.38	339.5	0.85	0.71	0.81	0.89	0.79	0.82
X-60×60×6.5×45°-200×200×10	0.37	373.5	0.94	0.78	0.90	0.92	0.89	0.91
X-60×60×8×45°-200×200×10	0.36	416.9	1.07	0.87	1.03	0.98	1.01	1.02
X-60×60×10×45°-200×200×10	0.34	438.8	1.14	0.92	1.11	0.97	1.08	1.09
X-60×60×3.33×45°-200×200×6.66	0.40	109.5	0.60	0.52	0.57	0.94	0.74	0.70
X-60×60×4.33×45°-200×200×6.66	0.39	113.6	0.63	0.54	0.60	0.91	0.78	0.73
X-60×60×5.33×45°-200×200×6.66	0.38	126.9	0.71	0.60	0.68	0.95	0.88	0.82
X-60×60×6.66×45°-200×200×6.66	0.37	133.9	0.76	0.63	0.73	0.94	0.95	0.87
X-60×60×2.5×45°-200×200×5	0.40	46.5	0.45	0.39	0.43	0.97	0.82	0.65
X-60×60×3.25×45°-200×200×5	0.40	47.9	0.47	0.40	0.44	0.93	0.86	0.67
X-60×60×4×45°-200×200×5	0.39	48.4	0.48	0.41	0.45	0.89	0.87	0.68
X-60×60×5×45°-200×200×5	0.38	52.2	0.52	0.44	0.50	0.88	0.95	0.74
X-60×130×6×25°-200×200×12	0.50	804.4	1.20	0.99	1.10	0.95	0.99	1.01
X-60×130×7.8×25°-200×200×12	0.48	906.8	1.38	1.12	1.27	1.02	1.15	1.16
X-60×130×9.6×25°-200×200×12	0.47	936.2	1.46	1.16	1.34	1.01	1.22	1.21
X-60×130×12×25°-200×200×12	0.42	1011.1	1.66	1.25	1.56	1.09	1.42	1.36
X-60×130×5×25°-200×200×10	0.51	459.9	0.98	0.82	0.89	0.90	0.87	0.87
X-60×130×6.5×25°-200×200×10	0.50	507.7	1.10	0.90	1.00	0.94	0.98	0.97
X-60×130×8×25°-200×200×10	0.48	580.5	1.28	1.03	1.17	1.02	1.15	1.12
X-60×130×10×25°-200×200×10	0.47	616.2	1.39	1.10	1.28	1.02	1.26	1.21
X-60×130×3.33×25°-200×200×6.66	0.52	153.9	0.72	0.62	0.65	0.99	0.85	0.77
X-60×130×4.33×25°-200×200×6.66	0.51	158.1	0.75	0.63	0.68	0.95	0.89	0.80
X-60×130×5.33×25°-200×200×6.66	0.51	176.1	0.84	0.70	0.77	0.99	1.00	0.89
X-60×130×6.66×25°-200×200×6.66	0.49	177.0	0.86	0.71	0.79	0.93	1.03	0.91
X-60×130×2.5×25°-200×200×5	0.53	67.4	0.55	0.48	0.50	1.06	0.97	0.73
X-60×130×3.25×25°-200×200×5	0.52	69.0	0.57	0.49	0.52	1.01	1.00	0.75
X-60×130×4×25°-200×200×5	0.52	72.0	0.60	0.51	0.55	0.99	1.06	0.79
X-60×130×5×25°-200×200×5	0.51	71.5	0.61	0.51	0.55	0.91	1.06	0.79
X-75×90×6×40°-200×200×12	0.53	801.5	1.14	1.01	1.04	0.89	0.94	1.02
X-75×90×7.8×40°-200×200×12	0.51	870.6	1.27	1.10	1.16	0.91	1.05	1.12
X-75×90×9.6×40°-200×200×12	0.50	934.8	1.40	1.18	1.28	0.94	1.16	1.22
X-75×90×12×40°-200×200×12	0.45	955.4	1.52	1.20	1.41	0.97	1.28	1.30
X-75×90×5×40°-200×200×10	0.54	443.6	0.90	0.81	0.81	0.81	0.80	0.85
X-75×90×6.5×40°-200×200×10	0.52	514.1	1.06	0.93	0.96	0.89	0.95	0.99
X-75×90×8×40°-200×200×10	0.51	560.6	1.18	1.02	1.08	0.92	1.06	1.10
X-75×90×10×40°-200×200×10	0.50	646.8	1.40	1.17	1.28	1.00	1.25	1.29
X-75×90×3.33×40°-200×200×6.66	0.55	159.1	0.71	0.65	0.64	0.95	0.83	0.80
X-75×90×4.33×40°-200×200×6.66	0.54	166.3	0.75	0.68	0.68	0.93	0.88	0.85
X-75×90×5.33×40°-200×200×6.66	0.53	180.7	0.83	0.74	0.75	0.95	0.97	0.93
X-75×90×6.66×40°-200×200×6.66	0.52	191.7	0.89	0.78	0.81	0.94	1.05	0.99
X-75×90×2.5×40°-200×200×5	0.56	67.5	0.53	0.49	0.48	0.99	0.91	0.74
X-75×90×3.25×40°-200×200×5	0.55	69.0	0.55	0.50	0.49	0.94	0.95	0.76
X-75×90×4×40°-200×200×5	0.55	70.5	0.56	0.51	0.51	0.90	0.98	0.78
X-75×90×5×40°-200×200×5	0.54	75.5	0.61	0.55	0.55	0.90	1.06	0.85
X-90×90×6×45°-200×200×12	0.59	875.3	1.13	1.02	1.01	0.85	0.91	1.00
X-90×90×7.8×45°-200×200×12	0.57	972.0	1.29	1.13	1.16	0.89	1.05	1.13
X-90×90×9.6×45°-200×200×12	0.56	1060.8	1.45	1.24	1.30	0.93	1.18	1.26
X-90×90×12×45°-200×200×12	0.51	1111.0	1.63	1.30	1.48	0.98	1.34	1.38
X-90×90×5×45°-200×200×10	0.59	520.7	0.95	0.87	0.85	0.83	0.83	0.90
X-90×90×6.5×45°-200×200×10	0.58	584.1	1.10	0.98	0.98	0.88	0.96	1.02
X-90×90×8×45°-200×200×10	0.57	677.3	1.30	1.14	1.16	0.97	1.14	1.20
X-90×90×10×45°-200×200×10	0.55	730.0	1.44	1.23	1.30	0.99	1.27	1.32

X-90×90×3.33×45°-200×200×6.66	0.61	177.0	0.71	0.67	0.63	0.93	0.82	0.80
X-90×90×4.33×45°-200×200×6.66	0.60	186.6	0.76	0.70	0.68	0.91	0.88	0.85
X-90×90×5.33×45°-200×200×6.66	0.59	208.2	0.86	0.79	0.77	0.96	1.00	0.96
X-90×90×6.66×45°-200×200×6.66	0.58	224.0	0.95	0.85	0.85	0.96	1.10	1.05
X-90×90×2.5×45°-200×200×5	0.62	81.2	0.57	0.55	0.51	1.05	0.97	0.80
X-90×90×3.25×45°-200×200×5	0.61	85.0	0.61	0.57	0.54	1.02	1.03	0.84
X-90×90×4×45°-200×200×5	0.60	86.3	0.62	0.58	0.55	0.97	1.06	0.86
X-90×90×5×45°-200×200×5	0.59	89.5	0.66	0.60	0.58	0.93	1.12	0.90
X-120×120×6×45°-200×200×12	0.80	1391.2	1.00	1.22	0.86	0.83	0.78	0.93
X-120×120×7.8×45°-200×200×12	0.78	1635.0	1.25	1.44	1.08	0.92	0.98	1.13
X-120×120×9.6×45°-200×200×12	0.77	1825.3	1.47	1.60	1.27	0.99	1.15	1.31
X-120×120×12×45°-200×200×12	0.72	1885.9	1.77	1.66	1.53	1.02	1.39	1.49
X-120×120×5×45°-200×200×10	0.81	848.1	0.84	1.07	0.73	0.83	0.72	0.84
X-120×120×6.5×45°-200×200×10	0.79	943.8	0.99	1.19	0.86	0.88	0.84	0.96
X-120×120×8×45°-200×200×10	0.78	1171.1	1.29	1.48	1.12	1.03	1.10	1.24
X-120×120×10×45°-200×200×10	0.77	1313.2	1.55	1.66	1.33	1.09	1.31	1.44
X-120×120×3.33×45°-200×200×6.66	0.82	318.9	0.67	0.91	0.58	1.03	0.75	0.81
X-120×120×4.33×45°-200×200×6.66	0.81	383.1	0.84	1.09	0.72	1.15	0.94	1.00
X-120×120×5.33×45°-200×200×6.66	0.80	404.8	0.92	1.15	0.79	1.15	1.03	1.08
X-120×120×6.66×45°-200×200×6.66	0.79	435.4	1.04	1.24	0.89	1.15	1.16	1.19
X-120×120×2.5×45°-200×200×5	0.83	154.6	0.56	0.78	0.48	1.22	0.93	0.84
X-120×120×3.25×45°-200×200×5	0.82	164.8	0.61	0.83	0.53	1.21	1.02	0.92
X-120×120×4×45°-200×200×5	0.82	174.5	0.67	0.88	0.58	1.20	1.11	0.99
X-120×120×5×45°-200×200×5	0.81	184.9	0.74	0.94	0.64	1.18	1.22	1.07
X-50×100×4×27°-150×150×6	0.53	184.4*	1.07	0.89	0.97	1.11	1.09	1.03
X-50×100×4×63°-150×150×6	0.70	266.9*	1.09	1.29	0.95	1.08	1.07	1.25
X-50×100×4×27°-120×120×4	0.64	112.8*	1.33	1.17	1.17	1.37	1.57	1.36
X-50×100×4×63°-120×120×4	0.87	218.4*	1.33	2.24	1.13	1.55	1.27	1.69
X-50×100×4×27°-120×120×3	0.68	64.9*	1.03	0.99	0.90	1.23	1.62	1.27
X-50×100×4×63°-120×120×3	0.87	136.3*	1.29	2.06	1.09	1.65	1.53	1.80
X-80×80×4×45°-120×120×4	0.85	191.7*	1.10	1.50	0.96	1.44	1.24	1.32
X-80×80×4×45°-140×140×4	0.75	120.1*	0.97	1.04	0.84	1.21	1.29	1.19
X-80×80×4×45°-120×120×3	0.87	126.5*	1.17	1.43	1.01	1.57	1.48	1.41
		Mean (P_m)	0.99	0.90	0.90	1.04	1.06	1.01
		COV (V_p)	0.345	0.394	0.352	0.160	0.187	0.232
		Resistance factor (ϕ)	1.00	1.00	1.00	0.80	0.80	0.70
		Reliability index (β_0)	1.16	0.79	0.85	2.57	2.51	2.53

Note: * data obtained from Pandey and Young [2].

Table 7. Values of coefficients for BR T- and X-joints unified design equation.

Joint Types	Coefficients						
	A	B	C	D	E	F	G
BR T-joint	2	1	0.7	0.6	0.01	0.5	0.02
BR X-joint	2.3	0.6	0.7	0.4	0.017	0.5	0.02